POLITECNICO DI TORINO
Repository ISTITUZIONALE

Modeling Excitable Cells with Memristors

Original
Modeling Excitable Cells with Memristors / Maheshwar, S.; Ascoli, A.; Tetzlaff, R.; Rajamani, V.; Budhathoki, R. K.. - In: JOURNAL OF LOW POWER ELECTRONICS AND APPLICATIONS. - ISSN 2079-9268. - ELETTRONICO. - (2024).

Availability:
This version is available at: 11583/2988905 since: 2024-05-22T08:31:37Z

Publisher:
MDPI

Published
DOI:

Terms of use:

This article is made available under terms and conditions as specified in the corresponding bibliographic description in the repository

Publisher copyright

(Article begins on next page)

29 June 2024

Journal of
Low Power Electronics and Applications

MDPI

Article

Modeling Excitable Cells with Memristors

Maheshwar Sah [1,2*], Alon Ascoli [3], Ronald Tetzlaff [4*], Vetriveeran Rajamani [5] and Ram Kaji Budhathoki [6]

[1] Department of Electronics and Communication Engineering, Nepal Engineering College, Changunarayan, Bhaktapur, , Nepal, e-mail: sahmaheshwar@gmail.com
[2] TJX Evansville, Indiana, USA
[3] Department of Electronics and Telecommunications, Politecnico di Torino, 10129 Turin, Italy; e-mail: alon.ascoli@polito.it
[4] Faculty of Electrical and Computer Engineering, Institute of Circuits and Systems, Technische Universität Dresden, Dresden, Germany; e-mail: ronald.tetzlaff@tu-dresden.de
[5] School of Electronics Engineering (SENSE), Vellore Institute of Technology, Vellore, Tamilnadu, India; e-mail: vetriece86@gmail.com
[6] Department of Electrical and Electronics Engineering, Kathmandu University, Dhulikhel, Kavre, Nepal; e-mail: ramkaji@gmail.com
* Correspondence: tetzlaff@tu-dresden.de; sahmaheshwar@gmail.com

Abstract: This paper presents an in-depth analysis of an excitable membrane of a biological system by proposing a novel approach that the cells of excitable membrane can be modeled as the networks of memristors. We provide compelling evidence from the Chay neuron model that the *state-independent mixed ion-channel* behaves as a nonlinear resistor, while the state-dependent *voltage-sensitive potassium ion-channel* and *calcium-sensitive potassium ion-channel* function as generic memristors from the perspective of electrical circuit theory. The mechanism to give the rise to the periodic oscillation, aperiodic (chaotic) oscillation, spikes and bursting in an excitable cell are also analyzed via small-signal model, pole-zero diagram of admittance functions, local activity, edge of chaos and Hopf bifurcation theorem. It is also proved that the zeros of the admittance functions are equivalent to the eigen values of the Jacobian matrix and the presence of the positive real parts of the eigen values between the two bifurcations points lead to the generation of complicated electrical signals in an excitable membrane. The innovative concepts outlined in this paper pave the way for a deeper understanding of the dynamic behavior of excitable cells, offering potent tools for simulating and exploring the fundamental characteristics of biological neurons.

Keywords: Memristor; excitable cell; oscillation; chaos; spikes; bursting; Chay model; small-signal model; pole-zero diagram; local activity; edge of chaos; Hopf bifurcation

Citation: To be added by editorial staff during production.

Academic Editor: Firstname Lastname

Received: date
Revised: date
Accepted: date
Published: date

Copyright: © 2024 by the authors. Submitted for possible open access publication under the terms and conditions of the Creative Commons Attribution (CC BY) license (https://creativecommons.org/licenses/by/4.0/).

1. Introduction

The electrical activities of neurons are characterized by a diverse array of dynamic phenomena, such as action potential, oscillation, spike, chaos and bursting. Understanding these qualitative features are essential for unraveling the principles underlying neuronal excitability. The popular Hodgkin-Huxley (HH) model developed in 1952 consists of membrane voltage, potassium conductance, sodium conductance and leakage conductance, provide a framework for understanding the propagation of action potential based on the squid giant axon experiments [1]. Recent analysis revealed that the potassium ion-channel and sodium ion-channel in the HH model, initially interpreted as time-varying conductances are in fact generic memristors from the perspective of electrical circuit theory [2-5]. The HH model has spurred significant interests to design electrical circuit models and observe the experimental results in the wide varieties of complex system of the membrane potential, nervous system, barnacle giant muscle fiber, Purkinje fibers, solitary hair cells, auditory periphery, mini review of neuromorphic architectures and implementation, organic synapses for neuromorphic electronics, and photochromic compounds [6-

16]. Similarly, extensive researches have been conducted to observe the varieties of oscillations in pancreatic β-cells inspired by the HH model [17-26]. The mathematical model of an excitable membrane in pancreatic β–cells consist of voltage-sensitive channels that allow the Na^+ and Ca^{2+} to enter the cell and, voltage-sensitive K^+ channels and voltage-insensitive K+ channel which allow to leave K^+ ion and activate intracellular calcium ion respectively [27-29]. Therefore, the outward current carried by K^+ ions pass through the voltage and calcium-sensitive channels, and inward current carried by Na^+ and Ca^{2+} ions pass through the voltage-sensitive Na^+ and Ca^{2+} channels. However, the above models consist of complicated nonlinear differential equations associated with membrane voltage. Later a modified model was presented by Chay [30], assuming the β-cells of the voltage-sensitive Na^+ conductance is almost inactive, and the inward current is almost exclusively carried by Ca^{2+} ions through the voltage-sensitive Ca^{2+} channel. Therefore, the assumption of a mixed effective conductance was formulated without affecting the results by expressing the total inward current in terms of a single mixed conductance g_I, and reversal potential E_I of the two functionally independent Na^+ and Ca^{2+} channels. The model consists of three nonlinear differential equations in contrast to the other complicated models of an excitable membrane of pancreatic β-cell. Our studies in this paper typically focus on the simplified Chay neuron model of an excitable cell [30].

The scientific novelty of this study is to model the excitable cells using memristive theory. By characterizing the state-independent voltage-sensitive mixed ion channel g_I as a nonlinear resistor, and the state-dependent voltage-sensitive potassium ion-channel $g_{K,V}$ and calcium-sensitive potassium ion-channel $g_{K,Ca}$ as time-invariant memristors in the Chay neuron model, this research introduces a novel approach to study the behavior of ion channels in excitable cells. This unique modeling framework extends memristive theory to the realm of neuroscience, opening up new avenues for investigating the complex dynamics of excitable cells and their role in neural information processing. Moreover, the study employs comprehensive analytical tools such as small signal equivalent circuit model, pole-zero diagrams, the local activity principle, edge of chaos theory, and Hopf bifurcation theorem with the goal of gaining deeper insights in to the dynamic behavior the excitable cells. By integrating these analytical tools, the study provides a comprehensive perspective on the dynamic behavior of excitable cells in the framework of memristive theory, potentially uncovering new insights and relationships that were previously unexplored. The contributions of the study have the potential to advance our understanding of excitable cell dynamics and their implications for neural function.

The paper is organized as follows. We introduce the Chay neuron model and its comparison analyses with HH, FitzHugh-Nagumo and Morris-Lecar(ML) models in section 2. Section 3 describes the pinched hysteresis fingerprints of ion-channel memristors. Section 4 presents Direct Current (DC) analysis of Memristive Chay neuron model**.** Section 5 provides the small-signal analysis. Section 6 explores the application of the local activity principle, edge of chaos theorem, and Hopf bifurcations in memristive Chay neuron. Finally, section 7 concludes the paper.

2. Chay Neuron Model of an Excitable Cell

Excitable cells are specialized cells in the body and neurons that are capable of generating electrical signals in response to certain stimuli. These cells are crucial for the functioning of various physiological processes, including nerve signaling, muscle contraction, and hormone release. Excitability in these cells is primarily due to the presence of specialized proteins called ion-channels in their cell membranes. These ion

channels control the movement of ions such as sodium (Na^+), potassium (K^+), calcium (Ca^{2+}), and chloride (Cl^-) across the membrane, leading to changes in the cell's membrane potential and the generation of electrical signals. The study of excitable cells encompasses a wide array of topics, and our primary aim is to present a unified model for both neuronal and secretory excitable membranes based on the Chay neuron model. The Chay neuron model, which focuses on a simplified representation of neuronal and secretory excitable membranes, aims to provide a unified framework for understanding the complex electrical activity observed in excitable cells. This model typically involves just three ordinary differential equations(ODEs) to capture the essential features of an excitable cell membrane. The model consists of (a) mixed ion-channel g_I (b) the state-dependent voltage-sensitive potassium ion-channel $g_{K,V}$ (c) calcium-sensitive potassium ion-channel $g_{K,Ca}$ and (d) leakage channel are described by the following differential equation:

$$\frac{dV}{dt} = \frac{I - g_I m_\infty^3 h_\infty (V - E_I) - g_{K,V} n^4 (V - E_K) - g_{K,\mathrm{Ca}} \frac{Ca}{1+Ca} (V - E_K) - g_\mathrm{L} (V - E_L)}{C_m} \quad \text{(1a)}$$

$$\frac{dn}{dt} = \frac{n_\infty - n}{\tau_n} \quad \text{(1b)}$$

$$\frac{dCa}{dt} = -\rho \left[m_\infty^3 h_\infty (V - E_{Ca}) + k_{Ca} Ca \right] \quad \text{(1c)}$$

where

$$n_\infty = \frac{\alpha_n}{\alpha_n + \beta_n},\ \alpha_n = \frac{0.01(V+20)}{1 - e^{-0.1(V+20)}},\ \beta_n = 0.125 e^{\left(\frac{-(V+30)}{80}\right)} \quad \text{(1d)}$$

$$m_\infty = \frac{\alpha_m}{\alpha_m + \beta_m},\ \alpha_m = \frac{0.1(V+25)}{1 - e^{-0.1(V+25)}},\ \beta_m = 4 e^{\left(\frac{-(V+50)}{18}\right)} \quad \text{(1e)}$$

$$h_\infty = \frac{\alpha_h}{\alpha_h + \beta_h},\ \alpha_h = 0.07 e^{\left(\frac{-(\mathrm{V}+50)}{20}\right)},\ \beta_h = \frac{1}{1 + e^{-0.1(V+20)}},\ \tau_n = \frac{1}{\lambda_n (\alpha_n + \beta_n)} \quad \text{(1f)}$$

Fig. 1(a) shows the typical circuit of Chay model with external current stimulus, denoted as I[1]. It consists of membrane potential V of capacitance C_m, potentials E_I, E_K and E_L for mixed Na^+-Ca^{2+} ions, K^+ and leakage ions respectively. The conductances g_I, $g_{K,V}$, $g_{K,Ca}$, and g_L, represent the *voltage-sensitive mixed ion-channel*, *voltage-sensitive potassium ion-channel*, *calcium-sensitive potassium ion-channel* and *leakage channel* respectively. In the

[1]Electrical model is not given in the Chay paper [30]. We have designed a typical electrical circuit model following the differential equation of the membrane potential. The symbolic representation of the conductances and potentials are assumed in different notations compared to the original representation. Fig. 1(a) shows an electrical circuit model following the conventional assumption of HH model.

upcoming session, we will provide a rigorous proof that the state independent mixed ion-channel functions as a nonlinear resistor. However, the commonly held belief regarding state-dependent ion-channels exhibiting time-varying conductances is found to be conceptually incorrect from the perspective of electrical circuit theory. Contrary to this conventional assumption, these ion-channels do not adhere to time-varying conductance principles. Instead, they align more accurately with the characteristics of time-invariant generic memristors from a circuit theoretic standpoint. A rigorous proof will be demonstrated in the subsequent section. The parameters for this model are summarized in Table 1[2] and list of abbreviations of the model parameters are illustrated in Appendix. The comparison analyses of the HH model[1], FitzHugh-Nagumo model[31], ML model[8], and the Chay model[30] are sumarized in Table 2 along with their respective strengths and limitations. It is notable that each model possesses distinct advantages and drawbacks making them suitable for different research contexts and questions. The choice of model depends on the level of detail required, computational resources available, and specific phenomena under investigation. This study predominantly centers on the Chay neuron model of excitable cells.

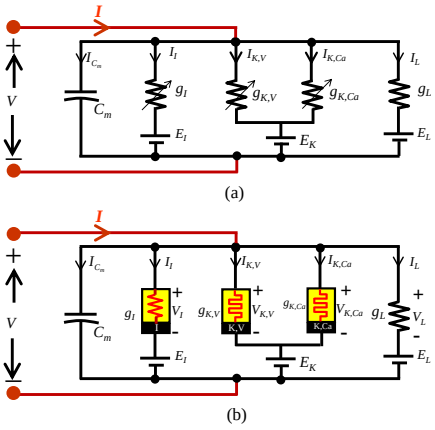

Figure 1. Typical Chay neuron model of an excitable cell [30]. (a) Electrical circuit model, following conventional assumption as time varying conductances [1]. (b) Equivalent memristive Chay model based on Chua's memristive theory [2-4]. The potential E_{Ca} for Ca^{2+} ion given in the rate of the calcium concentration in (1c) is not an external battery source and not shown in external Fig. 1(a) and Fig. 1(b), respectively.

[2] The unit of conductances of mixed ion-channel, voltage sensitive potassium ion-channel, calcium sensitive potassium ion-channel and leakage ion-channel in Chay model [30] are assumed as $g^* = \frac{conductance}{membrane\ capacitance} = \frac{mS/cm^2}{mF/cm^2} = \frac{1}{second(s)} = s^{-1}$. As, we are assuming the value of membrane capacitance $(C_m)=1mF/cm^2$, we use the unit of all the conductances of the ion-channels $g=mS/cm^2$ throughout this study, which is also the equivalent unit g* of original Chay model. Due to the periodic and dynamic nature of the conductance $g^*(g)$, it can also be considered as the "*conductance periodic factor*".

Table 1. Parameters of the Chay neuron model of an exctiable cell

C_m	$1mF/cm^2$	$g_{K,V}$	$1700\ mS/cm^2$
E_K	$-75\ mV$	g_I	$1800\ mS/cm^2$
E_I	$100\ mV$	g_L	$7\ mS/cm^2$
E_L	$-40\ mV$	$g_{K,Ca}$	$10\ mS/cm^2$
E_{Ca}	$100mV$	k_{Ca}	$3.3/18\ mV$
λ_n	230	ρ	0.27

Table 2. Comparision analyses of HH, FitzHugh-Nagumo, ML and Chay models

Models	Memristive Models	Strengths	Limitations
HH [1]	Potassium ion-channel and sodium ion-channel in the HH model are represented with generic memristors [3]	It is a framework to understand the emergence of action potential propagation in neuron based on the experimental data of squid giant axon.	Difficult to generalize to all neurons. Incapable of producing bursting
FitzHugh-Nagumo [31]	It doesn't follow the state dependent Ohm's law and can not model with memristors.	Simplified model of neuronal excitation.	Not accurately represent all neuronal behaviors. Incapable of producing bursting
ML [8]	Modeled that the state independent (dependent) calcium ion channel act as a nonlinear resistor(generic memristor) and state dependent potassium ion channels acts as a generic memristor [9-10].	Initially presented a model for the barnacle muscle fiber and later it is considered as a popular and simplified representation of the neuron model.	Limited in capturing certain neuronal dynamics. Can't produce bursting patterns.
Chay[30]	We are proposing a framework that the cells of excitable membranes can be modeled as the networks of memristors.	Novel model of excitable cells to capture multiple neuronal states, such as action potentials, periodic oscillations, aperiodic oscillations, spikes and bursting patterns.	Limited validation in experimental contexts and lack details for some applications.

3. Pinched Hysteresis Fingerprints of the Ion-Channel Memristor

A generic memristor driven by a current source or voltage source is a two-terminal electrical circuit element whose instantaneous current or voltage obeys a state-dependent Ohm's law. A generic memristor driven by a current source can be expressed as follows in terms of state $\dot{x}_n$:

$$v = R\left(x_1, x_2, ..., x_n\right) i \quad \text{(2a)}$$

$$\dot{x}_n = f_1(x_1, x_2, ..., x_n; i) \quad (2b)$$

where $R(\boldsymbol{x})$ is the memristance of the memristor and depends on "n" (n≥1) states variables,.

Similarly, a voltage-controlled memristor is defined in terms of the memductance $G(x)$ and the state variables $x_1, x_2 ..., x_n$, as follows:

$$i = G(x_1, x_2, ..., x_n)v \quad (3a)$$

$$\dot{x}_n = f_1(x_1, x_2, ..., x_n; v) \quad (3b)$$

Eqs. (2) and (3) play significant importances to distinguish the memristive and non-memristive system [32-33]. They provide evidence that the state independent *voltage-sensitive mixed ion-channel* functions as a nonlinear resistor and, state dependent *voltage-sensitive potassium ion-channel* and *calcium-sensitive potassium ion-channel* behaves as time-invariant generic memristors.

3.1. Voltage-sensitive mixed ion-channel nonlinear resistor

The time varying *voltage sensitive mixed ion-channel* with input voltage v_I and current i_I in the second element (from left) in Fig. 1(a) is given by,

$$V - E_I = v_I \quad (4a)$$

and

$$i_I = G_I(m_\infty, h_\infty)v_I \quad (4b)$$

and the conductance of the voltage sensitive mixed ion channel is given by

$$G_I(m_\infty, h_\infty) = g_I m_\infty^3 h_\infty \quad (4c)$$

where m_∞ *and* h_∞ are computed using (1e) and (1f)

$$m_\infty = \frac{0.1(v_I + E_I + 25)}{0.1(v_I + E_I + 25) + 4\left(1 - e^{-0.1(v_I + E_I + 25)}\right)e^{\left(\frac{-(v_I + E_I + 50)}{18}\right)}} \quad (4d)$$

$$h_\infty = \frac{0.07\left(1 + e^{-0.1(v_I + E_I + 20)}\right)e^{\left(\frac{-(v_I + E_I + 50)}{20}\right)}}{0.07\left(1 + e^{-0.1(v_I + E_I + 20)}\right)e^{\left(\frac{-(v_I + E_I + 50)}{20}\right)} + 1} \quad (4e)$$

Observe (4b)–(4e) are not identical to (2a)-2(b) or (3a)–(3b) in terms of state dependent Ohm's law. Consequently, the time-varying *voltage-sensitive mixed ion-channel* can be substituted by a nonlinear resistor[3] as depicted in the second element (from the left) in Fig. 1(b). To verify the *voltage-sensitive mixed ion-channel* is a nonlinear resistor, an extensive numerical simulation for a sinusoidal input voltage source $v_I = 100\sin(2\pi ft)$ *mV*

[3] Mixed ion-channel is a nonlinear voltage controlled resistor with conductance $G_I(m_\infty, h_\infty)$ where m_∞, and h_∞ are functions of the voltage v_I across the two-terminal element.

is performed for the three different frequencies namely, *f=100 Hz, 200 Hz*, and *1 KHz*, respectively. Fig. 2 shows the corresponding output nonlinear waveform on currente i_I *vs. voltage* v_I plane for these frequencies, confirming that the mixed ion-channel exhibits the properties of a nonlinear resistor only.

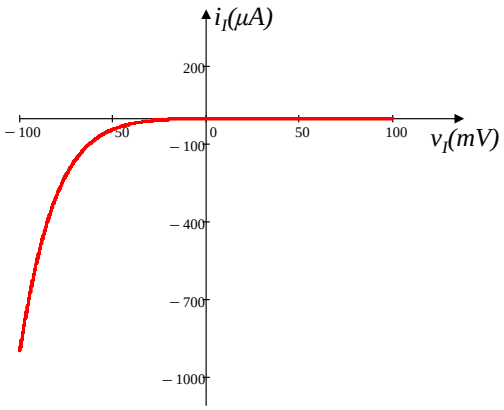

Figure 2. *Output waveform plotted on* i_I *vs.* v_I *plane when the input voltage* $v_I = 100\sin(2\pi ft)$ *mV* is applied with three different frequencies, namely *f = 100 Hz, 200 Hz, 1 KHz* to the *voltage-sensitive mixed ion-channel*. The output nonlinear waveform observed in Fig. 2 for different frequencies confirm the mixed ion channel is a nonlinear resistor.

3.2. Voltage-sensitive potassium ion-channel memristor

Let us define the voltage across the *voltage-sensitive potassium ion-channel* shown in third (from left) element in Fig. 1(a) is $v_{K,V}$ and current is $i_{K,V}$, then

$$V - E_K = v_{K,V} \tag{5a}$$

and current entering to the channel is

$$i_{K,V} = G_{K,v}(n)\, v_{K,V} \tag{5b}$$

where the memductance is given by

$$G_{K,V}(n) = g_{K,V}\, n^4 \tag{5c}$$

and the state equation describing the channel in terms of n can be simplified from 1(b) as,

$$\frac{dn}{dt} = f(n; v_{K,V}) = \lambda_n \left[\frac{0.01\left(v_{K,V} + E_K + 20\right)}{1 - e^{-0.1\left(v_{K,V} + E_K + 20\right)}} \left(1 - n\right) - 0.125\, e^{\left(\frac{-\left(v_{K,V} + E_K + 30\right)}{80}\right)} n \right] \tag{5d}$$

Note that (5b)-(5d) are identical to the voltage controlled generic memristor defined in (3a)-(3b) with first order differential equation. Hence, the time-varying conductance shown in Fig. 1(a) of voltage-*sensitive potassium ion-channel* is replaced with *voltage-sensitive potassium ion-channel* memristor as shown in the third element (from left) in Fig. 1(b).

We observed the memristive fingerprint of the *voltage-sensitive potassium ion-channel* memristor by applying sinusoidal bipolar signal under different frequencies. This

property asserts that beyond some frequency f^*, the pinched hysteresis loops characterized by a memristor shrinks to a single-valued function through the origin as frequency $f > f^*$ tends to infinity. To verify this property, a sinusoidal voltage source $v_{K,V}(t)=100\sin(2\pi ft)mV$ is applied to the *voltage-sensitive potassium ion-channel* with frequencies *f=100 KHz, 500 KHz,* and *4 MHz* respectively. As shown in Fig. 3, the zero crossing pinched hysteresis loops shrink as the frequencies increase and tend to a straight line at 4 *MHz* which confirms that the *voltage-sensitive potassium ion-channel* is a generic memristor. All of these pinched hysteresis loops exhibit the fingerprints of a memristor [33].

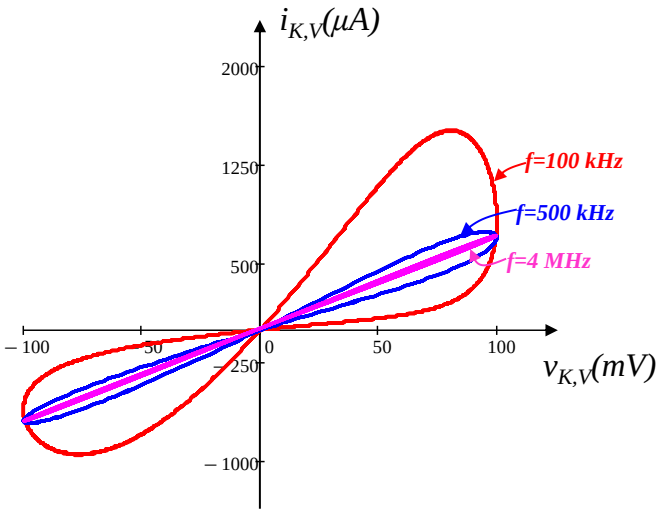

Figure 3. Pinched hysteresis loops of *voltage-sensitive potassium ion-channel* memristor at frequencies *f=100 KHz, 500 KHz, and 4 MHz* for the input signal $v_{K,V}(t) = 100\sin(2\pi ft)\ mV$.

3.3. *Calcium-sensitive potassium ion-channel memristor*

Let us consider the input voltage of the *calcium-sensitive potassium ion-channel*, the fourth element (from left) in Fig. 1(a) is $v_{K,Ca}$ [4] and current is $i_{K,Ca}$ then the current entering to the channel is given by

$$i_{K,\mathrm{Ca}} = G_{K,\mathrm{Ca}}(\mathrm{Ca})\, v_{K,\mathrm{Ca}} \tag{6a}$$

where

$$V - E_K = v_{K,\mathrm{Ca}} \tag{6b}$$

and the memductance of the calcium-sensitive potassium channel is given by

$$G_{K,\mathrm{Ca}}(\mathrm{Ca}) = g_{K,\mathrm{Ca}} \frac{Ca}{1+Ca} \tag{6c}$$

[4] Since the same potential E_K is shared by the *voltage-sensitive potassium ion-channel* memristor and *calcium- sensitive potassium ion-channel* memristor, the voltage assumed $V\text{-}E_K = v_{K,V}$ in (5a) and $V\text{-}E_K = v_{K,Ca}$ in (6b) are identical. The voltages $v_{K,V}$ and $v_{K,Ca}$ are assumed to distinguish the input voltage applied to *voltage-sensitive potassium ion-channel* memristor and *calcium- sensitive potassium ion-channel* memristor, respectively.

The state equation in terms of calcium concentration from 6(b) and (1c) is given by,

$$\frac{dCa}{dt} = f\left(Ca; V_{K,\mathrm{Ca}}\right) = -\rho\left[\, m_{\infty}^{3} h_{\infty}\left(v_{K,Ca} + E_K - E_{Ca}\right) + k_{Ca} Ca\right] \tag{6d}$$

Observe that (6b)–(6d) are examples of a voltage-controlled memristor defined in (3a)–(3b) in terms of the calcium concentration channel Ca. Since only one state equation is defined in terms of *Ca*, we call this memristor as a first order *calcium-sensitive potassium ion-channel* generic memristor. Therefore, the time varying *calcium-sensitive potassium ion-channel* is replaced with *calcium-sensitive potassium ion-channel* memristor as shown in the fourth element (from left) in Fig. 1(b).

Let us verify the fingerprint of the frequency-dependent pinched hysteresis loops of the *calcium-sensitive potassium ion-channel* by applying sinusoidal voltage source $v_{KCa}(t) = 100\sin(2\pi ft)\ mV$ with frequencies *f=10 Hz*, *30 Hz* and *200 Hz* respectively. Observe from Fig. 4 that, all the zero crossing pinched hysteresis loops shrink as the frequencies of the input signal increase and tend to a straight line for the frequency *f=200 Hz*. All of the pinched hysteresis fingerprint confirm that the *calcium-sensitive potassium ion-channel* is a generic memristor.

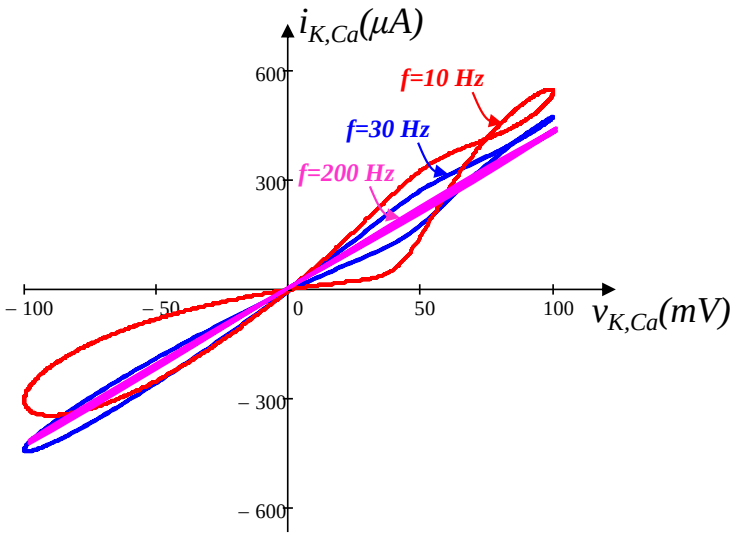

Figure 4. Pinched hysteresis loops of *calcium-sensitive potassium ion-channel memristor* at frequencies *f = 10Hz*, *30Hz* and *200Hz* for the input signal $v_{K,Ca}(t) = 100\sin(2\pi ft)\ mV$.

4. DC analysis of Memristive Chay Model of an Excitable Cell

The primary objectives to analyze the DC behavior of the memristive Chay model is to identify its equilibrium points of the nonlinear equations. These equilibrium points represent the steady-state solutions obtained by equating the rate of change of equilibrium voltage V_m, gate activation *n* of the *voltage-sensitive* p*otassium ion-channel* memristor and concentration of calcium-sensitive *Ca* of the *calcium sensitive potassium ion-channel* memristor to zero from (1a), (1b) and (1c) respectively. By determining these equilibrium points,

insights can be gained into the behavior of the excitable cell under different conditions, such as varying input stimuli or parameter values, and can be expressed as a function of current *I as:*

$$n = n_\infty(V_m) \triangleq \hat{n}(V_m) \tag{7a}$$

$$Ca = Ca_\infty(V_m) \triangleq C\hat{a}(V_m) \tag{7b}$$

$$I = g_I m_\infty^3 h_\infty \left(V_m - E_I\right) + g_{K,V}\hat{n}^4\left(V_m - E_K\right) + g_{K,Ca}\frac{C\hat{a}}{1+C\hat{a}}\left(V_m - E_K\right) + g_L\left(V_m - E_L\right) \tag{7c}$$

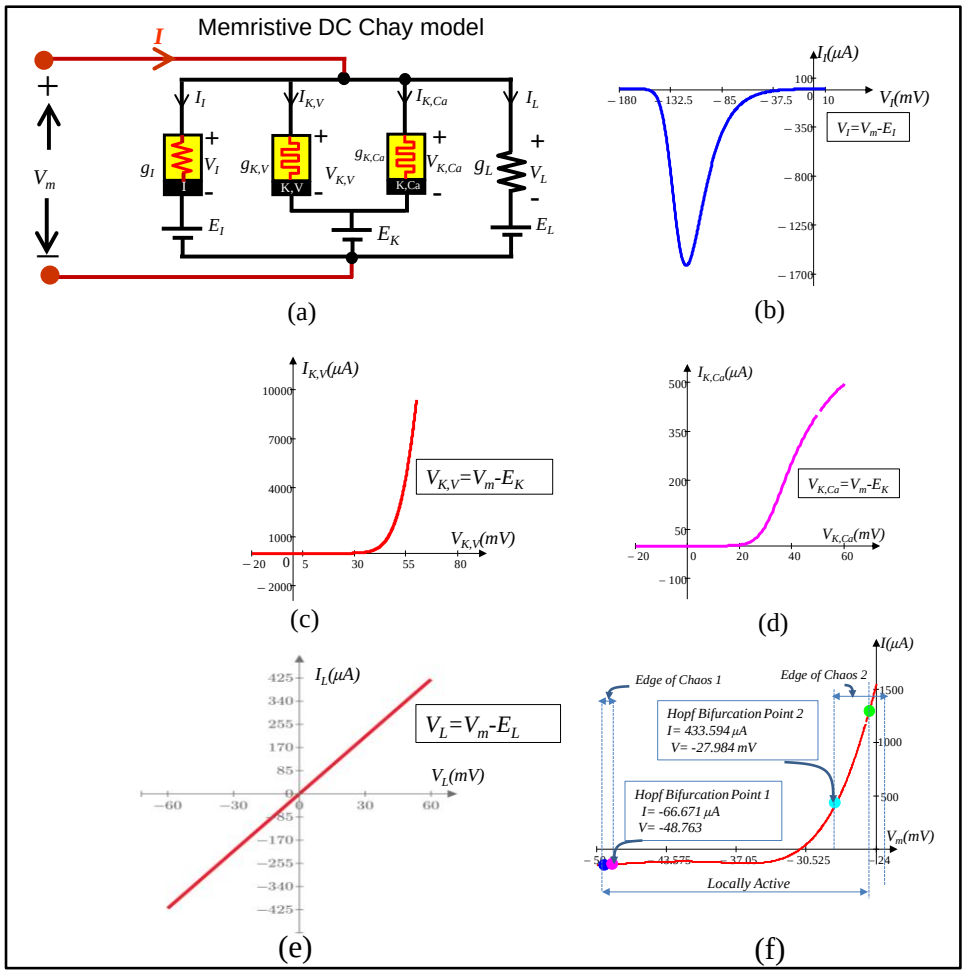

Figure 5. (a) Memristive DC Chay model at equilibrium voltage V_m. (b) *DC V-I* curve of mixed ion-channel nonlinear resistor at equilibrium voltage V_I=V_m-E_I. (c) DC *V-I* curve of voltage sensitive potassium ion-channel memristor at equilibrium voltage $V_{K,V}$=V_m-E_K. (d) DC *V-I* curve of calcium sensitive potassium ion-channel memristor at equilibrium voltage $V_{K,Ca}$=V_m-E_K. (e) DC *V-I* curve of leakage channel at equilibrium voltage V_L=V_m-*EL*.(f) Plot of *DC V-I* curve of memristive Chay model at membrane voltage V_m.

The external current *I* expressed as the function of membrane voltage V_m in (7c) gives the *explicit* formula of the DC *V-I* curve of the memristive Chay model. We have plotted

the individual DC *V-I* curve of voltage sensitive mixed ion channel non-linear resistor, voltage sensitive potassium ion-channel memristor, calcium sensitive potassium ion-channel memristor and leakage channel at equilibrium voltage V_I, $V_{K,V}$, $V_{K,Ca}$ and V_L as shown in the Fig. 5(b), Fig. 5(c), Fig. 5(d) and Fig. 5(e) respectively. Fig. 5(f) shows DC *V-I* curve of Fig. 5(a) over the range of DC voltage *-50 mV*$<V_m<$*-24 mV*. For any DC value of V_m, we calculated the corresponding value of *I* as the vertical axis. Our extensive calculations show that, the two Hopf bifurcation points occur at V_m=*-48.763 mV* (*resp.*, *I=-66.671* μA) and V_m=*-27.984 mV* (resp., *I=433.594* μA) respectively. Details of these two bifurcation points will be discussed in upcoming section

5. Small-Signal Circuit Model

The small-signal equivalent circuit is the linearized method to predict the response of electronic circuits when a small input signal is applied to an equilibrium point *Q*. The objective of this section is to analyze the small-signal response of *voltage-sensitive mixed ion-channel* nonlinear resistor, *voltage-sensitive potassium ion-channel* memristor and *calcium-sensitive potassium ion-channel* memristor using Taylor series expansion and Laplace transformation.

5.1. Small-signal circuit model of the mixed ion-channel nonlinear resistor

The small signal equivalent circuit of the *mixed ion-channel* nonlinear resistor at an equilibrium point Q_I [5] on the *DC* V_I-I_I curve is derived as follows

$$v_I = V_I(Q_I) + \partial v_I \tag{8a}$$

$$i_I = I_I(Q_I) + \partial i_I \tag{8b}$$

Applying Taylor series expansion to the *voltage-sensitive mixed ion-channel* nonlinear resistor defined in (8a)-(8b) at the DC operating point Q_I, we get

$$\begin{aligned} i_I &= f(V_I + \delta v_I) = a_{00}(Q_I) + a_{12}(Q_I)\delta v_I + h.o.t. \\ &= I_I(Q_I) + \delta i_I \end{aligned} \tag{8c}$$

Where *h.o.t* denotes higher order terms and coefficeints can be computed as,

$$a_{00}(Q_I) = G_I(Q_I)V_I(Q_I) = I_I(Q_I) \tag{8d}$$

$$a_{12}(Q_I) = \frac{\partial f(v_I)}{\partial v_I} \tag{8e}$$

Linearize (8c) by neglecting the h.o.t. then,

$$\delta i_I = a_{12}(Q_I)\delta v_I \tag{8f}$$

Taking the Laplace transform of (8f), we obtain

[5] The equilibrium point Q_I at v_I=V_I is obtained by solving 4(b).

$$\hat{i}_I(s) = a_{12}(Q_I)\hat{v}_I(s) \quad (8g)$$

The admittance $Y_I(s; Q_I)$ of the small-signal equivalent circuit of *the voltage sensitive mixed ion-channel* nonlinear resistor at the DC operating point Q_I is given by,

$$Y_I(s; Q_I) = \frac{\hat{i}_I(s)}{\hat{v}_I(s)} = a_{12}(Q_I) = \frac{1}{\frac{1}{a_{12}(Q_I)}} = \frac{1}{R_{1I}} \quad (8h)$$

where

$$R_{1,I} = 1/a_{12}(Q_I) \quad (8i)$$

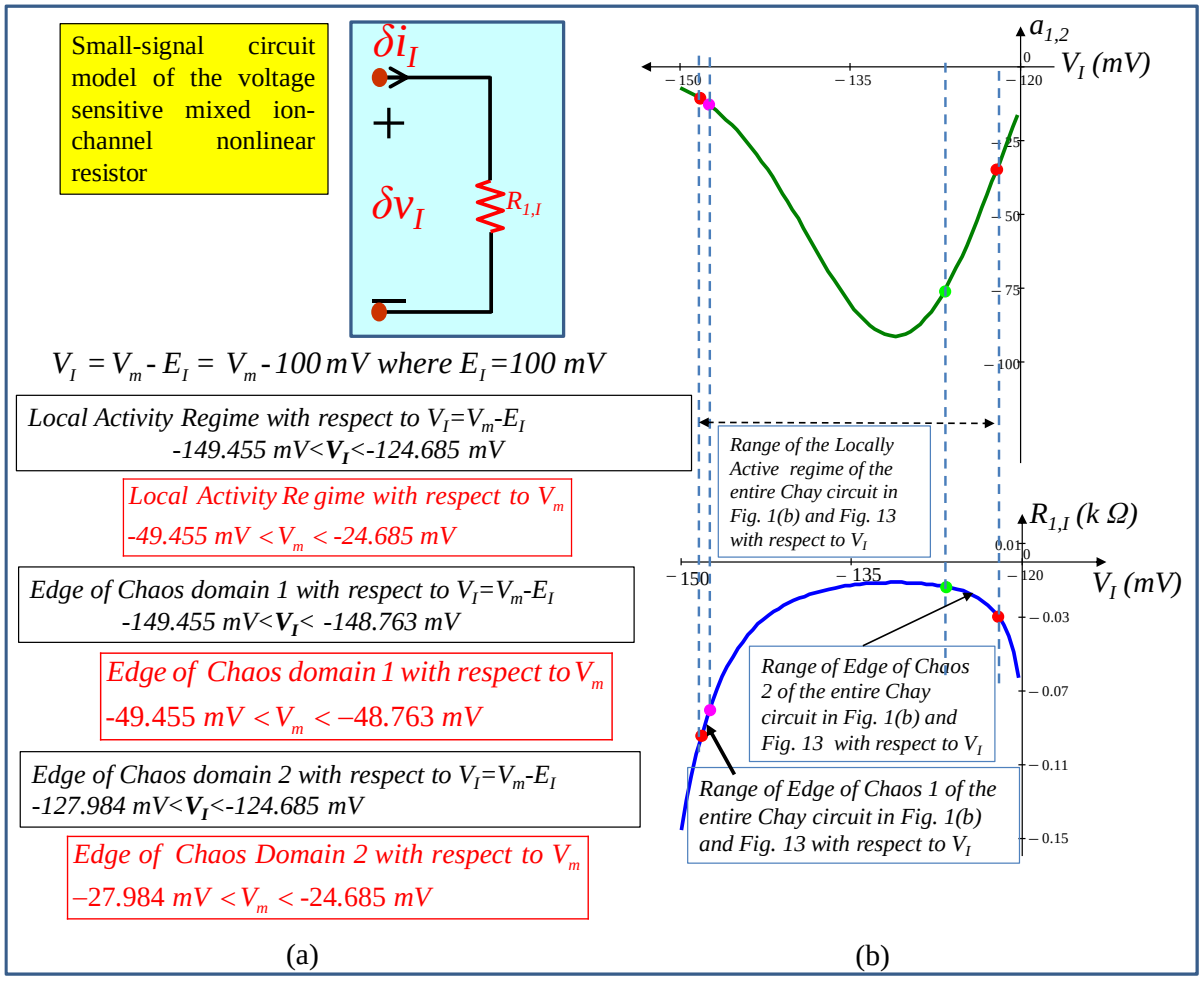

Figure 6. (a) Small-signal circuit model of the *voltage-sensitive mixed ion-channel* nonlinear resistor about the DC equilibrium point Q_I (V_I, I_I). (b) Plot of the coefficient a_{12} and resistance $R_{1,I}$ as a function of the DC equilibrium voltage $V_I = V_m - E_I$ where $E_I = 100\ mV$. $R_{1,I} < 0$ over the range of local activity, edge of chaos 1 and edge of chaos 2 of the mixed ion channel nonlinear resistor is identified with respect to V_I of the entire Chay circuit in Fig. 1(b) and Fig. 13 .

Table 3. Explicit formulas for computing the coefficients $a_{12}(Q_I)$ of the *voltage-sensitive mixed ion channel* nonlinear resistor

$$a_{12}(Q_I) = g_I\left[m(V_I)^3 h(V_I) + m(V_I)^3 V_I \frac{d_I h(V_I)}{dV_I} + h(V_I) V_I \frac{d_I m(V_I)^3}{dV_I}\right]$$

$$h(V_I) = \frac{\left(1+e^{-0.1(V_I+E_I+20)}\right)0.07e^{\left(\frac{-(V_I+E_I+50)}{20}\right)}}{\left(1+e^{-0.1(V_I+E_I+20)}\right)0.07e^{\left(\frac{-(V_I+E_I+50)}{20}\right)}+1}$$

$$R_{1,I} = 1/a_{12}(Q_I)$$

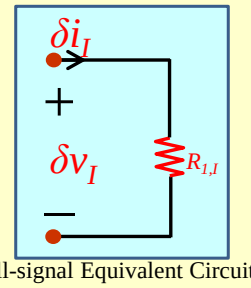

Small-signal Equivalent Circuit

$$h_d(V_I) = \frac{dh(V_I)}{dV_I} = -h(V_I)^2 \left(\frac{\frac{0.07}{20}\left(1+e^{-0.1(V_I+E_I+20)}\right)e^{\left(\frac{-(V_I+E_I+50)}{20}\right)} + 0.007e^{\left(\frac{-(V_I+E_I+50)}{20}\right)}e^{-0.1(V_I+E_I+20)}}{\left(\left(1+e^{-0.1(V_I+E_I+20)}\right)0.07e^{\left(\frac{-(V_I+E_I+50)}{20}\right)}\right)^2}\right)$$

$$m_d(V_I) = \frac{dm(V_I)^3}{dV_I} = 3m(V_I)^2 \frac{dm(V_I)}{dV_I} = 3m(V_I)^2 m_{dd}(V_I)$$

$$m(V_I) = \frac{0.1(V_I+E_I+25)}{0.1(V_I+E_I+25)+4\left(1-e^{-0.1(V_I+E_I+25)}\right)e^{\left(\frac{-(V_I+E_I+50)}{18}\right)}}$$

$$m_{dd}(V_I) = \frac{-40m_\infty^2}{(V_I+E_I+25)^2}\left((V_I+E_I+25)m_{ddd} - \left(1-e^{-0.1(V_I+E_I+25)}\right)e^{\left(\frac{-(V_I+E_I+50)}{18}\right)}\right)$$

$$m_{ddd}(V_I) = \frac{-1}{18}\left(1-e^{-0.1(V_I+E_I+25)}\right)e^{\left(\frac{-(V_I+E_I+50)}{18}\right)} + 0.1e^{\left(\frac{-(V_I+E_I+50)}{18}\right)}e^{-0.1(V_I+E_I+25)}$$

From (8h), it is followed that the small-signal admittance function of the *mixed ion-channel* nonlinear resistor is equivalent to a linear resistor. The corresponding small-signal equivalent circuit and a plot of the coefficient $a_{12}(Q_I)$ and resistance $R_{1,I}$ as a function of the DC equilibrium voltage $V_I = V_m - E_I$ *where* $E_I = 100$ *mV* are shown in Fig. 6(a) and Fig. 6(b), respectively. The explicit formulas for computing coefficient $a_{12}(Q_I)$ are given in Table 3 for readers' convenience.

5.2. Small-signal circuit model of the voltage-sensitive potassium ion-channel memristor

The small-signal circuit model of the *voltage sensitive potassium ion-channel* memristor at an equilibrium point $Q_{K,V}$[6] on the DC $V_{K,V}$-$I_{K,V}$ curve is derived by defining

$$n = n_{Q_{K,V}} + \delta n \tag{9a}$$

$$v_{K,V} = V_{K,V}(Q_{K,V}) + \delta v_{K,V} \tag{9b}$$

$$i_{K,V} = I_{K,V}(Q_{K,V}) + \delta i_{K,V} \tag{9c}$$

[6] The equilibrium point $Q_{K,V}$ at $v_{K,V} = V_{K,V}$ is obtained from (5d) by solving $f(n;V_{K,V}) = 0$ for $n = n_{K,V}$. The explicit formula for $n(V_{K,V})$ is given in Table 4.

Expanding $i_{K,V} = G_{K,V}(n)v_{K,V}$ from (5b) in a Taylor series about the equilibrium point $(N(Q_{K,V}), V_{K,V}(Q_{K,V}))$, we obtain,

$$\begin{aligned} i_{K,V} &= a_{00}(Q_{K,V}) + a_{11}(Q_{K,V})\,\delta n + a_{12}(Q_{K,V})\,\delta v_{K,V} + h.o.t. \\ &= I_{K,V}(Q_{K,V}) + \delta i_{K,V} \end{aligned} \tag{9d}$$

where

$$\delta n = n - n_{Q_{K,V}}, \qquad \delta v_{K,V} = v_{K,V} - V_{K,V}(Q_{K,V})$$

$$\delta i_{K,V} = i_{K,V} - I_{K,V}(Q_{K,V}) \tag{9e}$$

and

$$a_{00}(Q_{K,V}) = G_{K,V}\left(Q_{K,V}\right)V_{K,V}(Q_{K,V}) = I_{K,V}(Q_{K,V}) \tag{9f}$$

$$a_{11}(Q_{K,V}) = V_{K,V}(Q_{K,V})G'_{K,V}\left(n_{Q_{K,V}}\right) \tag{9g}$$

$$a_{12}(Q_{K,V}) = G_{K,V}\left(n_{Q_{K,V}}\right) \tag{9h}$$

and h.o.t denotes the higher-order terms. Let us linearize the nonlinear equation by neglecting the h.o.t. in (9d), then:

$$\delta i_K = a_{11}(Q_{K,V})\delta n + a_{12}(Q_{K,V})\delta v_{K,V} \tag{9i}$$

Similarly, expanding the state equation $f\left(n_{K,V}, V_{K,V}\right)$ in (5d) using a Taylor series about the equilibrium point $(n(Q_{K,V}), V_{K,V}(Q_{K,V}))$, we obtain

$$\begin{aligned} &f(n_{Q_{K,V}} + \delta n,\, V_{K,V}(Q_{K,V}) + \delta v_{K,V}) \\ &= f(n_{Q_{K,V}},\, V_{K,V}(Q_{K,V})) + b_{11}(Q_{K,V})\,\delta n + b_{12}(Q_{K,V})\,\delta v_{K,V} + h.o.t. \end{aligned} \tag{9j}$$

where

$$b_{11}(Q_{K,V}) = \left.\frac{\partial f_n\left(n,\, v_{K,V}\right)}{\partial n}\right|_{Q_{K,V}} \tag{9k}$$

$$b_{12}(Q_{K,V}) = \left.\frac{\partial f_N\left(n,\, v_{K,V}\right)}{\partial v_{K,V}}\right|_{Q_{K,V}} \tag{9l}$$

Linearizing the nonlinear state equation (9j) by neglecting the h.o.t., we get

$$\frac{d\left(\partial n\right)}{dt} = b_{11}(Q_{K,V})\,\delta n + b_{12}(Q_{K,V})\delta v_{K,V} \tag{9m}$$

Taking Laplace transform of (9i) and (9m), we obtain

$$\hat{i}_{K,V}(s) = a_{11}(Q_{K,V})\,\hat{n}(s) + a_{12}(Q_{K,V})\hat{v}_{K,V}(s) \quad \text{(9n)}$$

$$s\,\hat{n}(s) = b_{11}(Q_{K,V})\,\hat{n}(s) + b_{12}(Q_{K,V})\,\hat{v}_{K,V}(s) \quad \text{(9o)}$$

Solving (9o) for $\hat{n}(s)$ and substituting the result into (9n), we obtain the following admittance $Y_{K,V}(s;\ Q_{K,V})$ for the small-signal equivalent circuit of the *voltage sensitive potassium ion-channel* memristor at equilibrium point $Q_{K,V}$:

$$Y_{K,V}(s;\ Q_{K,V}) = \frac{\hat{i}_{K,V}(s)}{\hat{v}_{K,V}(s)} = \left[\frac{1}{\dfrac{s}{a_{11}(Q_{K,V})b_{12}(Q_{K,V})} - \dfrac{b_{11}(Q_{K,V})}{a_{11}(Q_{K,V})b_{12}(Q_{K,V})}} + \frac{1}{\dfrac{1}{a_{12}(Q_{K,V})}} \right] \quad \text{(9p)}$$

$$\boxed{Y_{K,V}\left(s;\ Q_{K,V}\right) = \left(\frac{1}{\left(sL_{K,V} + R_{1K,V}\right)} + \frac{1}{R_{2K,V}} \right)} \quad \text{(9q)}$$

where $L_{K,V} \triangleq \dfrac{1}{a_{11}(Q_{K,V})b_{12}(Q_{K,V})}$ (9r)

$$R_{1K,V} \triangleq -\frac{b_{11}(Q_{K,V})}{a_{11}(Q_{K,V})b_{12}(Q_{K,V})} \quad \text{(9s)}$$

$$R_{2K,V} \triangleq \frac{1}{a_{12}(Q_{K,V})} \quad \text{(9t)}$$

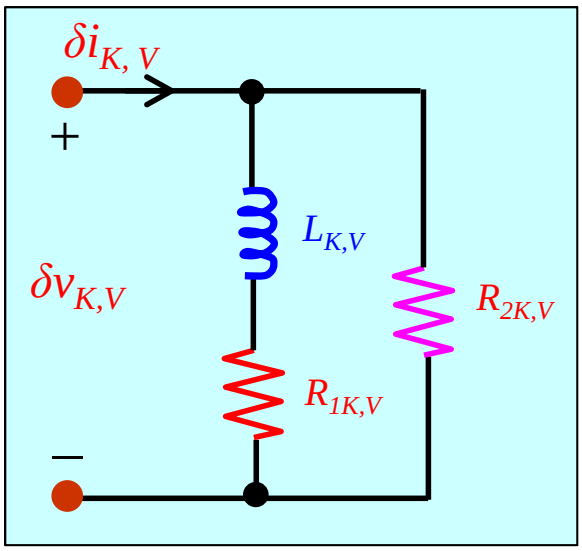

Figure 7. Small-signal equivalent circuit model of the *voltage-sensitive potassium ion-channel* memristor about the DC equilibrium point $Q_{K,V}$ ($V_{K,V}$, $I_{K,V}$).

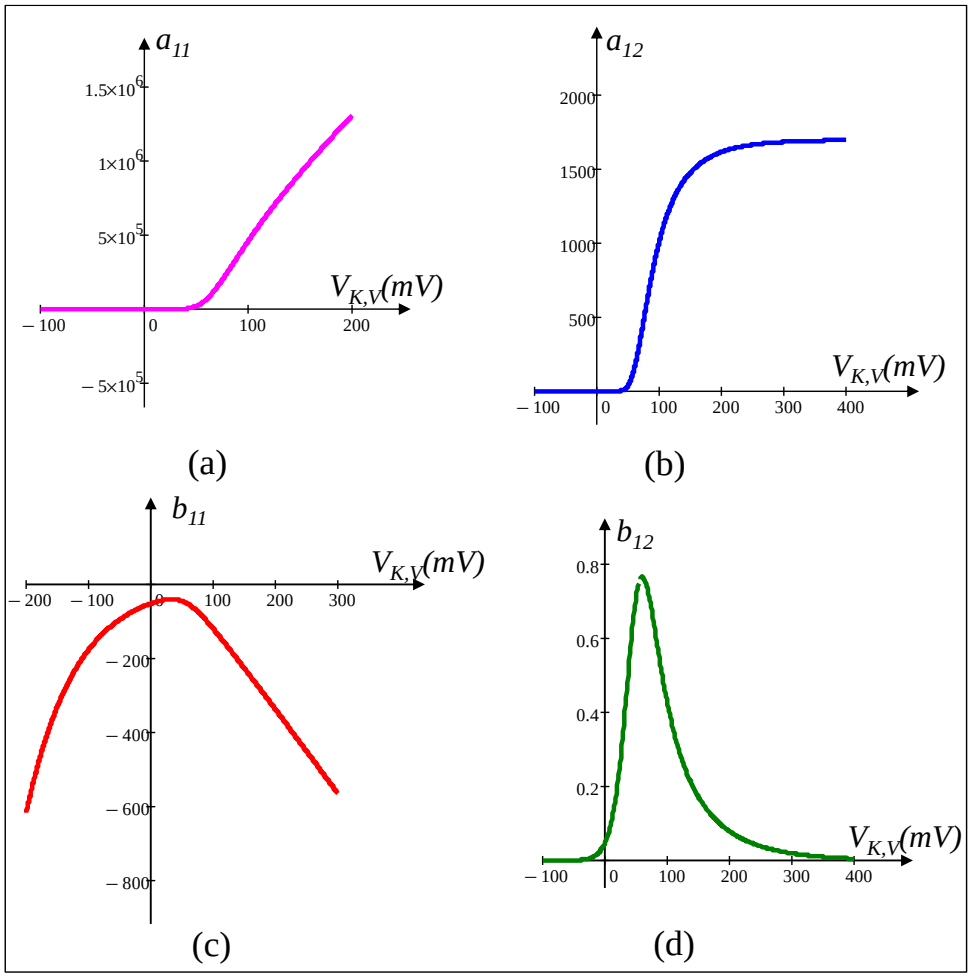

Figure 8. Plot of coefficients (a) a_{11} (b) a_{12} (c) b_{11} and (d) b_{12} of the voltage-sensitive potassium ion-channel memristor as a function of the DC equilibrium voltage $V_{K,V}$.

It follows from (9r)-(9t) that the small-signal admittance function of the first-order voltage sensitive *potassium ion-channel memristor* is equivalent to the series connection of an inductor and a resistor in parallel with another resistor as shown in Fig. 7. The corresponding coefficients a_{11}, a_{12}, b_{11}, b_{12} and *inductance* $L_{K,V}$, *resistance* $R_{1K,V}$ and *resistance* $R_{2K,V}$ as a function of the DC equilibrium voltage $V_{K,V}=V_m-E_K$ *where* E_K*=-75mV* are shown in Figs. 8 and Figs. 9, respectively. Please note that the local activity, edge of chaos 1 and edge of chaos 2 shown in Figs. 9 are not the local activity and edge of chaos domains of the separate two terminal of the voltage sensitive potassium ion-channel memristor. The small signal positive inductance and resistances *(i.e.* $L_{K,,V}>0$, $R_{1K,V}>0$ and, $R_{2K,V}>0$) of the potassium ion-channel memristor observed over the local activity, edge of chaos 1 and edge of chaos 2 regime are just corresponding range of the voltage with respect to $V_{K,V}$ of the entire connected Chay small-signal equivalent circuit of Fig. 1(b) and Fig. 13. For the readers' convenience, the explicit formulas for computing the coefficients $a_{11}(Q_{K,V})$, $a_{12}(Q_{K,V})$, $b_{11}(Q_{K,V})$, $b_{12}(Q_{K,V})$ and $L_{K,V}$, $R_{1K,V}$, $R_{2K,V}$ are summarized in Table 4.

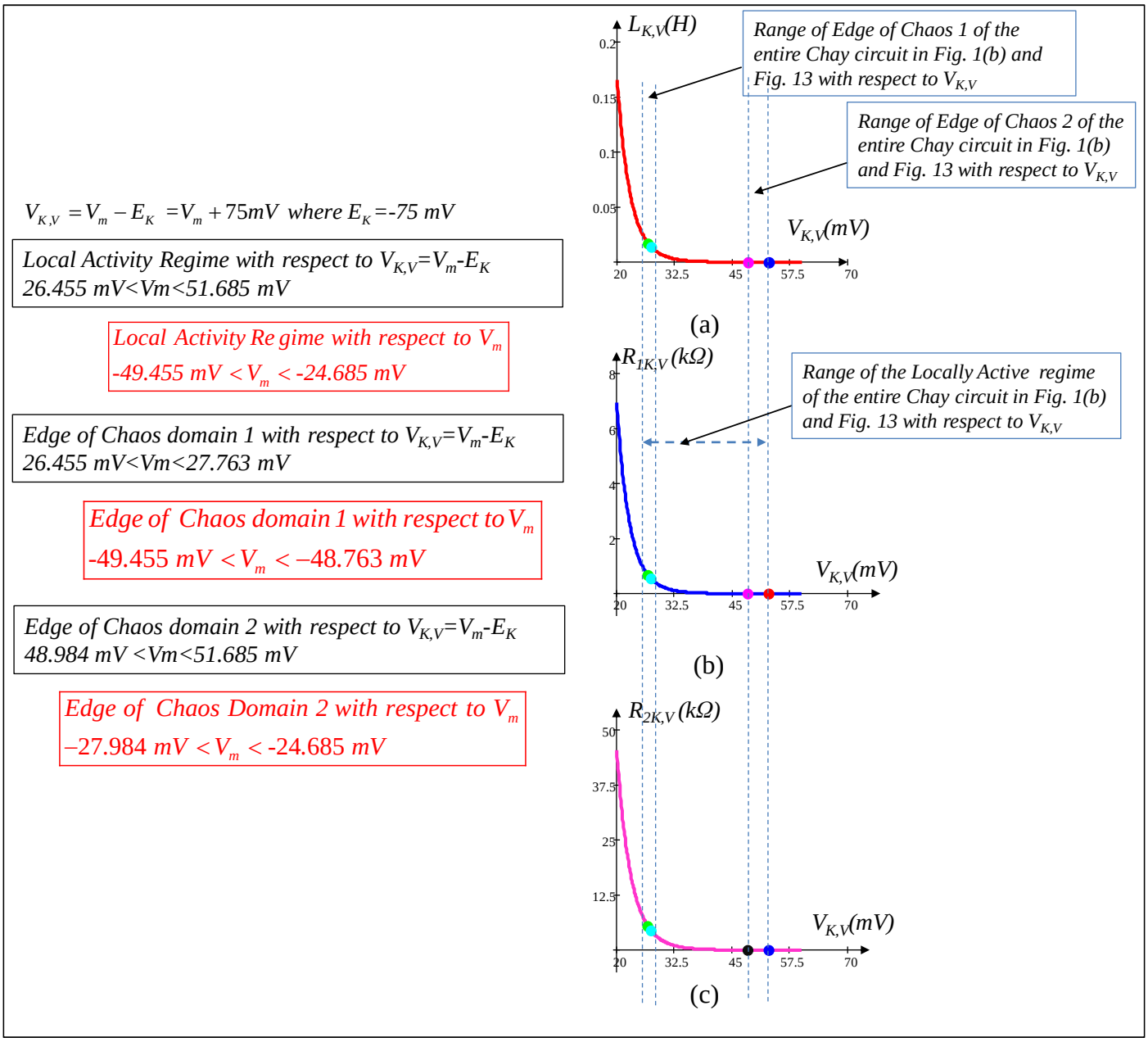

Figure 9. (a) Inductance $L_{K,V}$ (b) resistance $R_{1K,V}$ and (c) resistance $R_{2K,V}$ of the *voltage-sensitive potassium ion-channel* memristor as a function of DC equilibrium voltage $V_{K,V}=V_m-E_K$ *where* E_K=-75mV. $L_{K,V}$>0, R_{1KV}>0 and R_{2KV}>0 shown in figures over the local activity, edge of chaos 1 and edge of chaos 2 are just corresponding range of the voltage with respect to $V_{K,V}$ of the entire connected Chay small signal equivalent circuit of Fig. 1(b) and Fig. 13.

Table 4: Explicit formulas for computing the coefficients $a_{11}(Q_{K,V})$, $a_{12}(Q_{K,V})$, $b_{11}(Q_{K,V})$, $b_{12}(Q_{K,V})$ and $L_{K,V}$, $R_{1K,V}$, $R_{2K,V}$ of the *voltage sensitive potassium ion-channel* memristor.

$$a_{11}(Q_{K,V}) = 4g_{K,V}n^3(V_{K,V})V_{K,V} \qquad a_{12}(Q_{K,V}) = g_{K,V}n^4(V_{K,V}) \qquad n(V_{K,V}) = \frac{\alpha_n(V_{K,V})}{(\alpha_n(V_{K,V}) + \beta_n(V_{K,V}))}$$

$$\alpha_n(V_{K,V}) = \frac{0.01(V_{K,V} + E_K + 20)}{1 - e^{-0.1(V_{K,V}+E_K+20)}} \qquad L_{K,V} = \frac{1}{a_{11}(Q_{K,V})\, b_{12}(Q_{K,V})} \qquad R_{1K,V} = -\frac{b_{11}(Q_{K,V})}{a_{11}(Q_{K,V}) b_{12}(Q_{K,V})}$$

$$\beta_n(V_{K,V}) = 0.125e^{\left(\frac{-(V_{K,V}+E_K+30)}{80}\right)} \qquad b_{11}(Q_{K,V}) = -\lambda_n\left[\alpha_n(V_{K,V}) + \beta_n(V_{K,V})\right] \qquad R_{2K,V} = \frac{1}{a_{12}(Q_{K,V})}$$

$$b_{12}(Q_{K,V}) = \lambda_n\left[\left(\frac{0.01 - 0.1\alpha_n(V_{K,V})\, e^{-0.1(V_{K,V}+E_K+20)}}{\left(1 - e^{-0.1(V_{K,V}+E_K+20)}\right)}\right)(1 - n(V_{K,V})) + \frac{\beta_n(V_{K,V})}{80} n(V_{K,V})\right]$$

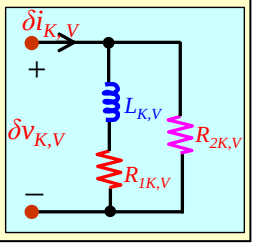

5.3. Small-signal circuit model of the calcium-sensitive potassium ion-channel memristor

The small-signal circuit model of the *calcium-sensitive potassium-channel* memristor at an equilibrium point $Q_{K,Ca}$[7] in the DC $V_{K,Ca}$-$I_{K,Ca}$ curve is derived by defining

$$Ca = Ca_{Q_{K,Ca}} + \delta Ca \tag{10a}$$

$$v_{K,Ca} = V_{K,Ca}(Q_{Ca}) + \delta v_{K,Ca} \tag{10b}$$

$$i_{K,Ca} = I_{K,Ca}(Q_{K,Ca}) + \delta i_{K,Ca} \tag{10c}$$

Expanding $i_{K,Ca} = G_{K,Ca}(\mathrm{Ca})v_{K,Ca}$ from (6a) in a Taylor series about the equilibrium point $(Ca(Q_{K,Ca}), V_{Ca}(Q_{K,Ca}))$, we obtain

$$\begin{aligned} i_{K,Ca} &= a_{00}(Q_{K,Ca}) + a_{11}(Q_{K,Ca})\delta Ca + a_{12}(Q_{K,Ca})\delta v_{K,Ca} + h.o.t. \\ &= I_{K,Ca}(Q_{Ca}) + \delta i_{K,Ca} \end{aligned} \tag{10d}$$

where

$$\delta Ca = Ca - Ca_{Q_{K,Ca}}, \qquad \delta v_{K,Ca} = v_{K,Ca} - V_{K,Ca}(Q_{K,Ca})$$

$$\delta i_{K,ca} = i_{K,Ca} - I_{K,Ca}(Q_{K,Ca}) \tag{10e}$$

and

$$a_{00}(Q_{K,Ca}) = G_{Ca}\left(Q_{K,Ca}\right)V_{Ca}(Q_{K,Ca}) = I_{K,Ca}(Q_{K,Ca}) \tag{10f}$$

$$a_{11}(Q_{K,Ca}) = V_{K,Ca}(Q_{K,Ca})G'_{K,Ca}\left(Ca_{Q_{K,Ca}}\right) \tag{10g}$$

[7] The equilibrium point $Q_{K,Ca}$ at $v_{K,Ca} = V_{K,Ca}$ is obtained from (6d) by solving $f(Ca;V_{K,Ca}) = 0$ for $Ca = Ca_{K,Ca}$. The explicit formula for $Ca(V_{K,Ca})$ is given in Table 5.

$$a_{12}(Q_{K,Ca}) = G_{K,Ca}\left(Ca_{Q_{\mathrm{K,Ca}}}\right) \tag{10h}$$

and h.o.t denotes the higher-order terms. Let us linearize the nonlinear equation by neglecting the h.o.t. in (10d) then:

$$\delta i_{\mathrm{K,C}a} = a_{11}(Q_{K,Ca})\delta Ca + a_{12}(Q_{K,Ca})\delta v_{K,Ca} \tag{10i}$$

Similarly, expanding the state equation $f\left(Ca_{K,Ca}, V_{K,Ca}\right)$ of (6d) in a Taylor series about the equilibrium point $(Ca(Q_{K,Ca}), V_{Ca}(Q_{K,ca}))$, we obtain

$$\begin{aligned} &f(Ca_{QK,_{Ca}} + \delta Ca,\, V_{K,Ca}(Q_{K,Ca}) + \delta v_{K,Ca}) \\ &= f(\mathrm{Ca}_{QK,_{Ca}},\, V_{Ca}(Q_{K,Ca})) + b_{11}(Q_{K,Ca})\,\delta Ca + b_{12}(Q_{K,Ca})\,\delta v_{K,Ca} + h.o.t. \end{aligned} \tag{10j}$$

where

$$b_{11}(Q_{K,Ca}) = \left.\frac{\partial f\left(\mathrm{Ca},\, v_{K,Ca}\right)}{\partial Ca}\right|_{Q_{\mathrm{K,Ca}}} \tag{10k}$$

$$b_{12}(Q_{K,Ca}) = \left.\frac{\partial f\left(Ca,\, v_{K,Ca}\right)}{\partial v_{K,Ca}}\right|_{Q_{K,Ca}} \tag{10l}$$

Linearizing the nonlinear state equation (10j) by neglecting the h.o.t., we get

$$\frac{d\left(\partial Ca\right)}{dt} = b_{11}(Q_{K,Ca})\,\delta Ca + b_{12}(Q_{K,Ca})\delta v_{K,Ca} \tag{10m}$$

Taking Laplace transform of (10i) and (10m), we obtain

$$\hat{i}_{K,Ca}(s) = a_{11}(Q_{K,Ca})C\hat{a}(s) + a_{12}(Q_{K,Ca})\hat{v}_{Ca}(s) \tag{10n}$$

$$s\ C\hat{a}(s) = b_{11}(Q_{K,Ca})C\hat{a}(s) + b_{12}(Q_{K,Ca})\hat{v}_{K,Ca}(s) \tag{10o}$$

Solving (10o) for $C\hat{a}(s)$ and substituting the result into (10n), we obtain the following admittance $Y_{K,Ca}(s;\, Q_{K,Ca})$ of the small-signal equivalent circuit of the *calcium sensitive potassium ion-channel* memristor at equilibrium point $Q_{K,Ca}$:

$$Y_{K,Ca}(s;\, Q_{K,Ca}) = \frac{\hat{i}_{K,Ca}(s)}{\hat{v}_{K,Ca}(s)} = \left[\frac{1}{\dfrac{s}{a_{11}(Q_{K,Ca})b_{12}(Q_{K,Ca})} - \dfrac{b_{11}(Q_{K,Ca})}{a_{11}(Q_{K,Ca})b_{12}(Q_{K,Ca})}} + \frac{1}{\dfrac{1}{a_{12}(Q_{K,Ca})}}\right] \tag{10p}$$

$$\boxed{Y_{Ca}\left(s;\, Q_{Ca}\right) = \left(\frac{1}{\left(sL_{K,Ca} + R_{1K,Ca}\right)} + \frac{1}{R_{2K,Ca}}\right)} \tag{10q}$$

where $L_{K,Ca} \triangleq \dfrac{1}{a_{11}(Q_{K,Ca})b_{12}(Q_{K,Ca})}$ (10r)

$$R_{1K,Ca} \triangleq -\frac{b_{11}(Q_{K,Ca})}{a_{11}(Q_{K,Ca})b_{12}(Q_{K,Ca})} \quad \text{(10s)}$$

$$R_{2K,Ca} \triangleq \frac{1}{a_{12}(Q_{K,Ca})} \quad \text{(10t)}$$

It follows from (10r)-(10t) that the small-signal admittance function of the first-order *calcium-sensitive potassium ion-channel memristor* is equivalent to the series connection of an inductor and a resistor in parallel with another resistor as shown in Fig. 10. The corresponding coefficients a_{11}, a_{12}, b_{11}, b_{12} and *inductance* $L_{K,Ca}$, *resistance* $R_{1K,Ca}$, and *resistance* $R_{2K,Ca}$ as a function of the DC equilibrium voltage $V_{K,Ca}$ are shown in Figs. 11 and Figs. 12, respectively. The small-signal inductance and resistances(i.e. $L_{K,Ca}>0$, $R_{1K,Ca}>0$ and $R_{2KCa}>0$) over the edge of chaos 1 and edge of chaos 2 with respect to the $V_{K,Ca}$ are shown in Fig. 12(a), Fig. 12(b) and Fig. 12(c) respectively. Please note that the local activity, edge of chaos 1 and edge of chaos 2 shown in Fig. 12(a), Fig. 12(b) and Fig. 12(c) are not the local activity, edge of chaos 1 and edge of chaos 2 of the individual calcium sensitive potassium ion channel memristor. The local activity, edge of chaos domains are just an information showing the corresponding range of voltage with respect to $V_{K,Ca}$ when measured across the individual calcium sensitive potassium ion channel memristor of the entire connected Chay small-signal equivalent circuit of Fig. 1(b) and Fig. 13. For the readers' convenience, the explicit formulas for computing the coefficients $a_{11}(Q_{,K,Ca})$, $a_{12}(Q_{K,Ca})$, $b_{11}(Q_{,K,Ca})$, $b_{12}(Q_{,K,Ca})$ and $L_{K,Ca}$, $R_{1K,Ca}$, $R_{2K,Ca}$ are summarized in Table 5.

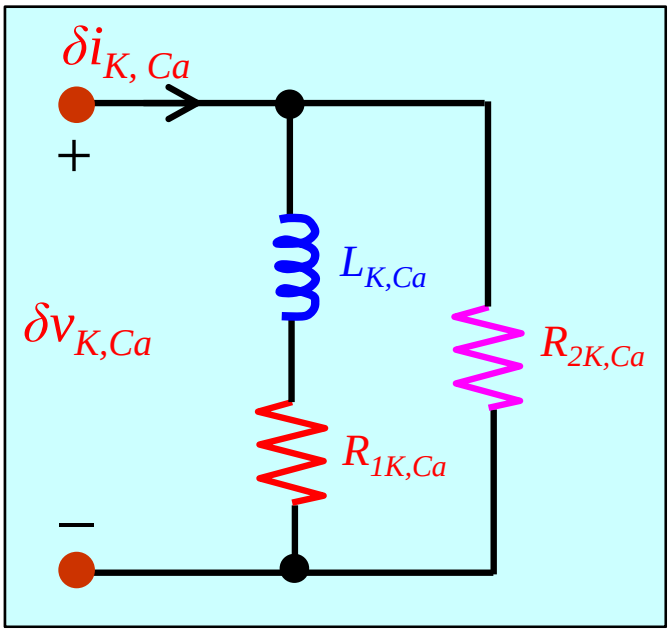

Figure 10. Small-signal equivalent circuit model of the *calcium-sensitive potassium ion-channel memristor* about the DC equilibrium point $Q_{K,Ca}$ ($V_{K,Ca}$, $I_{K,Ca}$).

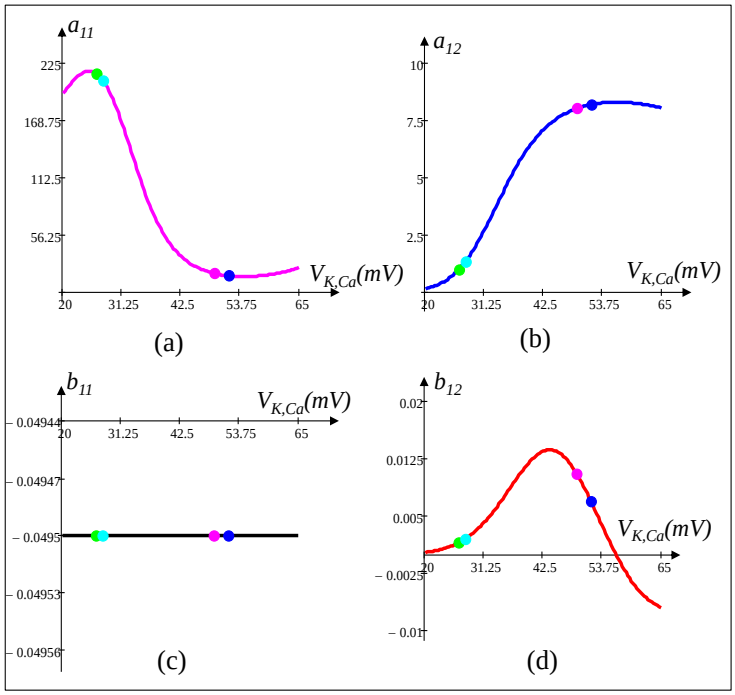

Figure 11. Plot of coefficients (a) a_{11} (b) a_{12} (c) b_{11} and (d) b_{12} of the *calcium-sensitive potassium ion-channel* memristor as a function of the DC equilibrium voltage $V_{K,Ca}$.

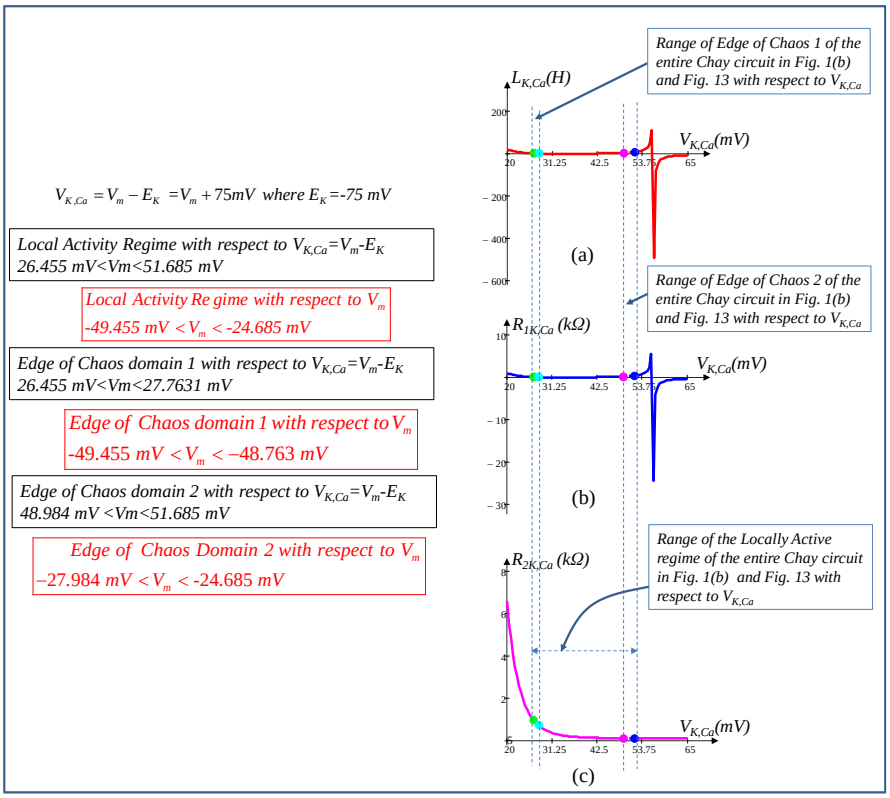

Figure 12. (a) Inductance $L_{K,Ca}$ (b) resistance $R_{1K,Ca}$ and (c) resistance $R_{2K,Ca}$ of the *calcium-sensitive potassium ion-channel memristor* as a function of DC equilibrium voltage $V_{K,Ca}$. $L_{K,Ca}>0$, $R_{1K,Ca}>0$ and $R_{2KCa}>0$ over the edge of chaos 1 and edge of chaos 2 with respect to $V_{K,Ca}$ of the entire connected Chay small-signal equivalent circuit of Fig.1(b) and Fig. 13.

Table 5: Explicit formulas for computing the coefficients $a_{11}(Q_{K,Ca})$, $a_{12}(Q_{K,Ca})$, $b_{11}(Q_{K,Ca})$, $b_{12}(Q_{K,Ca})$ and $L_{K,Ca}$, $R_{1K,Ca}$, $R_{2K,Ca}$ of the *calcium-sensitive potassium ion-channel* memristor.

$$m\left(V_{K,Ca}\right)=\frac{0.1\left(V_{K,Ca}+E_K+25\right)}{0.1\left(V_{K,Ca}+E_K+25\right)+4\left(1-e^{-0.1\left(V_{K,Ca}+E_K+25\right)}\right)e^{\left(\frac{-\left(V_{K,Ca}+E_K+50\right)}{18}\right)}}$$

$$h\left(V_{K,Ca}\right)=\frac{\left(1+e^{-0.1\left(V_{K,Ca}+E_K+20\right)}\right)0.07e^{\left(\frac{-\left(V_{K,Ca}+E_K+50\right)}{20}\right)}}{\left(1+e^{-0.1\left(V_{K,Ca}+E_K+20\right)}\right)0.07e^{\left(\frac{-\left(V_{K,Ca}+E_K+50\right)}{20}\right)}+1}$$

$$Ca\left(V_{K,Ca}\right)=\frac{-m^3\left(V_{K,Ca}\right)h\left(V_{K,Ca}\right)\left(V_{K,Ca}+E_K-E_{Ca}\right)}{k_{Ca}}$$

$$a_{11}\left(Q_{K,Ca}\right)=\frac{g_{K,Ca}V_{K,Ca}}{\left(1+Ca\left(V_{K,Ca}\right)\right)^2}$$

$$a_{12}\left(Q_{K,Ca}\right)=g_{K,Ca}\frac{Ca\left(V_{K,Ca}\right)}{1+Ca\left(V_{K,Ca}\right)}$$

$$b_{11}\left(Q_{K,Ca}\right)=-\rho k_{Ca}$$

$$b_{12}\left(Q_{K,Ca}\right)=-\rho\left[m^3\left(V_{K,Ca}\right)h\left(V_{K,Ca}\right)+m^3\left(V_{K,Ca}\right)\left(V_{K,Ca}+E_K-E_{Ca}\right)\frac{dh\left(V_{K,Ca}\right)}{dV_{K,Ca}}+h\left(V_{K,Ca}\right)\left(V_{K,Ca}+E_K-E_{Ca}\right)\frac{dm^3\left(V_{K,Ca}\right)}{dV_{K,CaI}}\right]$$

$$h_d\left(V_{K,Ca}\right)=\frac{dh\left(V_{K,Ca}\right)}{dV_{K,Ca}}=-h\left(V_{K,Ca}\right)^2\left(\frac{\frac{0.07}{20}\left(1+e^{-0.1\left(V_{K,Ca}+E_K+20\right)}\right)e^{\left(\frac{-\left(V_{K,Ca}+E_K+50\right)}{20}\right)}+0.007e^{\left(\frac{-\left(V_{K,Ca}+E_K+50\right)}{20}\right)}e^{-0.1\left(V_{K,Ca}+E_K+20\right)}}{\left(\left(1+e^{-0.1\left(V_{K,Ca}+E_K+20\right)}\right)0.07e^{\left(\frac{-\left(V_{K,Ca}+E_K+50\right)}{20}\right)}\right)^2}\right)$$

$$m_d\left(V_{K,Ca}\right)=\frac{dm^3\left(V_{K,Ca}\right)}{dV_{K,Ca}}=3m^2\left(V_{K,Ca}\right)\frac{dm\left(V_{K,Ca}\right)}{dV_I}=3m^2\left(V_{K,Ca}\right)m_{dd}\left(V_{K,Ca}\right)$$

$$m_{dd}\left(V_{K,Ca}\right)=\frac{-40m^2\left(V_{K,Ca}\right)}{\left(V_{K,Ca}+E_K+25\right)^2}\left(\left(V_{K,Ca}+E_K+25\right)m_{ddd}\left(V_{K,Ca}\right)-\left(1-e^{-0.1\left(V_{K,Ca}+E_K+25\right)}\right)e^{\left(\frac{-\left(V_{K,Ca}+E_K+50\right)}{18}\right)}\right)$$

$$m_{ddd}\left(V_{K,Ca}\right)=\frac{-1}{18}\left(1-e^{-0.1\left(V_{K,Ca}+E_K+25\right)}\right)e^{\left(\frac{-\left(V_{K,Ca}+E_K+50\right)}{18}\right)}+0.1e^{\left(\frac{-\left(V_{K,Ca}+E_K+50\right)}{18}\right)}e^{-0.1\left(V_{K,Ca}+E_K+25\right)}$$

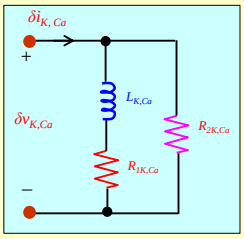

$$L_{K,Ca}=\frac{1}{a_{11}\left(Q_{K,Ca}\right)b_{12}\left(Q_{K,Ca}\right)}$$

$$R_{1K,Ca}=-\frac{b_{11}\left(Q_{K,Ca}\right)}{a_{11}\left(Q_{K,Ca}\right)b_{12}\left(Q_{K,Ca}\right)}$$

$$R_{2K,Ca}=\frac{1}{a_{12}\left(Q_{K,Ca}\right)}$$

5.4. Small-signal circuit model of the memristive Chay model

Let us replace the voltage-sensitive mixed ion-channel nonlinear resistor, the voltage-sensitive potassium ion-channel memristor, and the calcium-sensitive potassium ion-channel memristor in the memristive Chay neuron circuit of Fig. 1(b) with their small-signal models about DC operating voltages $V_I=V_m-E_I$, $V_{K,V}=V_m-E_K$, and $V_{K,Ca}=V_m-E_K$, respectively. Short-circuiting all the batteries, the equivalent small-signal circuit model of the third-order neuron circuit from Fig. 1(b) about the operating point $V_m(Q$ is found to be composed of one capacitor, two inductors, and six resistors as shown in Fig. 13. The local admittance $Y(s;V_m(Q))$ of this linear circuit seen from the port and formed by the capacitor terminals about Q is given by

$$Y(s;V_m(Q))=sC_m+\frac{1}{sL_{K,V}+R_{1K,V}}+\frac{1}{sL_{K,Ca}+R_{1K,ca}}+\frac{1}{R_{1,I}}+\frac{1}{R_{2K,V}}+\frac{1}{R_{2K,Ca}}+G_L \qquad (11)$$

The corresponding range of local activity, edge of chaos 1 and edge of chaos 2 at equilibrium voltage $V_m(Q)$ (*resp. I*) are also given in Fig. 13 for readers' convenience. We will cover the details of these regimes in the section on locally activity and edge of chaos. The circuit element $R_{1,I}$ is obtained by calculating the small signal model of the voltage-sensitive mixed ion-channel nonlinear resistor from Table 3 at equilibrium voltage

$V_m(Q)=V_I+E_I$. Similarly, $L_{K,V}$, $R_{1K,V}$, and $R_{2K,V}$ are calculated from the small-signal equivalent circuit of the *voltage sensitive potassium ion-channel memristor* from Table 4 and $L_{K,Ca}$, $R_{1K,Ca}$, and $R_{2K,Ca}$ are calculated from the small signal equivalent circuit of the *calcium-sensitive potassium ion channel memristor* from Table 5 at equilibrium voltage $V_m(Q)$ respectively. Note that $V_{K,V}+E_K$ and $V_{K,Ca}+E_K$ must be replaced by $V_m(Q)$ in Table 4 and Table 5 by the small signal model of the *voltage-sensitive potassium ion-channel memristor* and *calcium-sensitive potassium ion-channel memristor*, respectively.

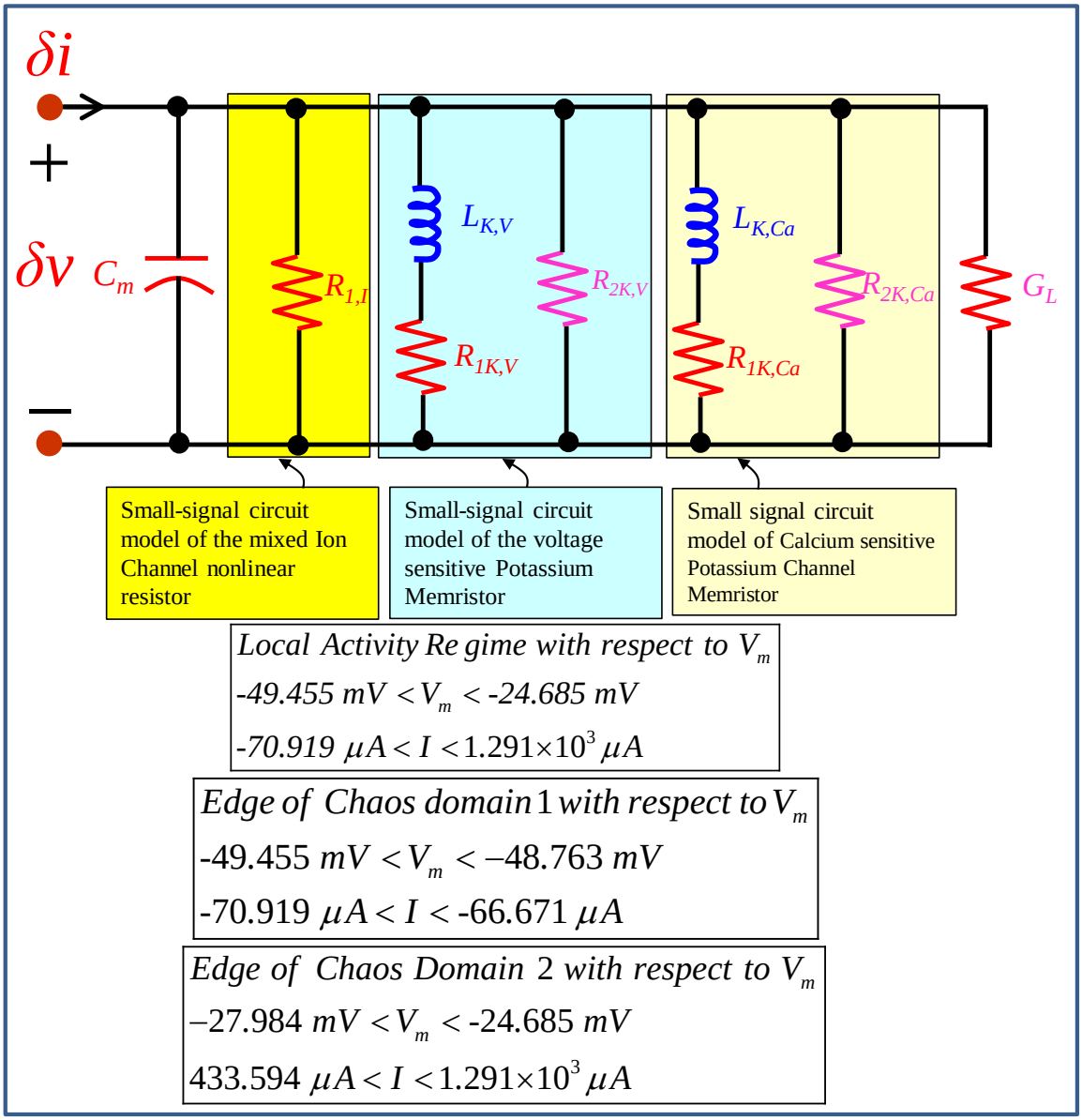

Figure 13. Small-signal equivalent circuit model of the memristive Chay model. The DC equilibrium voltage V_m is computed at $V_m=V_I+E_I$ for mixed ion channel non-linear resistor, $V_m=V_{K,V}+E_K$ for voltage sensitive potassium ion-channel memristor and $V_m=V_{K,Ca}+E_K$ for calcium sensitive potassium ion-channel memristor, respectively.

Table 6: Explicit formulas for computing the coefficients of $Y(s;Vm(Q))$.

$$b_3 = L_{K,V}L_{K,Ca}R_{1,I}R_{2K,V}R_{2K,Ca}C_m$$

$$b_2 = \left(L_{K,V}R_{1K,ca} + L_{K,Ca}R_{1K,V}\right)R_{1,I}R_{2K,V}R_{2K,Ca}C_m + L_{K,V}L_{K,Ca}R_{2K,V}R_{2K,Ca} + L_{K,V}L_{K,Ca}R_{1,I}R_{2K,Ca} + L_{K,V}L_{K,Ca}R_{1,I}R_{2K,V} + L_{K,V}L_{K,Ca}R_{1,I}R_{2K,V}R_{2K,Ca}G_L$$

$$b_1 = R_{1,I}R_{1K,V}R_{1K,ca}R_{2K,V}R_{2K,Ca}C_m + \left(L_{K,Ca}R_{1,I}R_{2K,V}R_{2K,Ca}\right) + \left(L_{K,V}R_{1,I}R_{2K,V}R_{2K,Ca}\right) + \left(L_{K,V}R_{1K,ca} + L_{K,Ca}R_{1K,V}\right)R_{2K,V}R_{2K,Ca} + \left(L_{K,V}R_{1K,ca} + L_{K,Ca}R_{1K,V}\right)R_{1,I}R_{2K,Ca} + \left(L_{K,V}R_{1K,ca} + L_{K,Ca}R_{1K,V}\right)R_{1,I}R_{2K,V} + \left(L_{K,V}R_{1K,ca} + L_{K,Ca}R_{1K,V}\right)R_{1,I}R_{2K,V}R_{2K,Ca}G_L$$

$$b_0 = R_{1,I}R_{1K,ca}R_{2K,V}R_{2K,Ca} + R_{1,I}R_{1K,V}R_{2K,V}R_{2K,Ca} + R_{1K,V}R_{1K,ca}R_{2K,V}R_{2K,Ca} + R_{1,I}R_{1K,V}R_{1K,ca}R_{2K,Ca} + R_{1,I}R_{1K,V}R_{1K,ca}R_{2K,V} + R_{1,I}R_{1K,V}R_{1K,ca}R_{2K,V}R_{2K,Ca}G_L$$

$$a_2 = L_{K,V}L_{K,Ca}R_{1,I}R_{2K,V}R_{2K,Ca}$$

$$a_1 = \left(L_{K,V}R_{1K,ca} + L_{K,Ca}R_{1K,V}\right)R_{1,I}R_{2K,V}R_{2K,Ca}$$

$$a_0 = R_{1,I}R_{1K,V}R_{1K,ca}R_{2K,V}R_{2K,Ca}$$

$$Y(s;V_m(Q)) = \frac{b_3s^3 + b_2s^2 + b_1s + b_0}{a_2s^2 + a_1s + a_0}$$

5.4.1. *Frequency Response*

A convenient way to find the total admittance $Y(s; Vm(Q))$ by recasting (11) into a rational function of the complex frequency variable s, is as follows:

$$Y(s;V_m(Q)) = \frac{b_3s^3 + b_2s^2 + b_1s + b_0}{a_2s^2 + a_1s + a_0} \quad \text{(12a)}$$

where the explicit formulas for computing the coefficients b_3, b_2, b_1, b_0, a_2, a_1, and a_0 are summarized in Table 6.

Substituting $s = i\omega$ in (12a), we obtain the following small-signal admittance function at the equilibrium voltage $V_m(Q)$:

$$Y(i\omega;V_m(Q)) = \frac{(b_0 - b_2\omega^2)(a_0 - a_2\omega^2) + a_1\omega^2(b_1 - b_3\omega^2)}{(a_0 - a_2\omega^2)^2 + (a_1\omega)^2} + i\omega\left[\frac{\left[(b_1 - b_3\omega^2)(a_0 - a_2\omega^2) - a_1(b_0 - b_2\omega^2)\right]}{(a_0 - a_2\omega^2)^2 + (a_1\omega)^2}\right] \quad \text{(12b)}$$

The corresponding *real part Re Y (iω; Vm(Q))* and *imaginary part Im Y (iω; Vm(Q))* from (12b) are given by,

$$\mathrm{Re}\,Y(i\omega;V_m(Q)) = \left[\frac{(b_0 - b_2\omega^2)(a_0 - a_2\omega^2) + a_1\omega^2(b_1 - b_3\omega^2)}{(a_0 - a_2\omega^2)^2 + (a_1\omega)^2}\right]$$

$$\mathrm{Im}\,Y(i\omega;V_m(Q)) = \omega\left[\frac{\left[(b_1 - b_3\omega^2)(a_0 - a_2\omega^2) - a_1(b_0 - b_2\omega^2)\right]}{(a_0 - a_2\omega^2)^2 + (a_1\omega)^2}\right] \quad \text{(12c)}$$

Fig. 14(a) and Fig. 14(b) show *ReY(iω; V_m(Q)) vs. ω*, *Im Y(iω; V_m(Q)) vs. ω*, and the Nyquist plot *Im Y(iω; V_m(Q)) vs. Re Y(iω; V_m(Q))* at the DC equilibrium voltage V_m= *-48.763 mV(resp., I=-66.671 μA)*, and V_m=*-27.984 mV(resp.*, I=*433.594 μA)*, respectively. Observe from Fig. 14(a) and Fig. 14(b) that *ReY(iω; V_m(Q))<0*, thereby confirming the memristive Chay model is a *locally active* at each of the two operating points. Our extensive numerical computations show the two DC equilibria coincide with two-Hopf bifurcation points are the origin of generating the oscillation, spikes, chaos and bursting in excitable cells. We will discuss about these two bifurcation points in next section with pole-zeros and eigen values diagram.

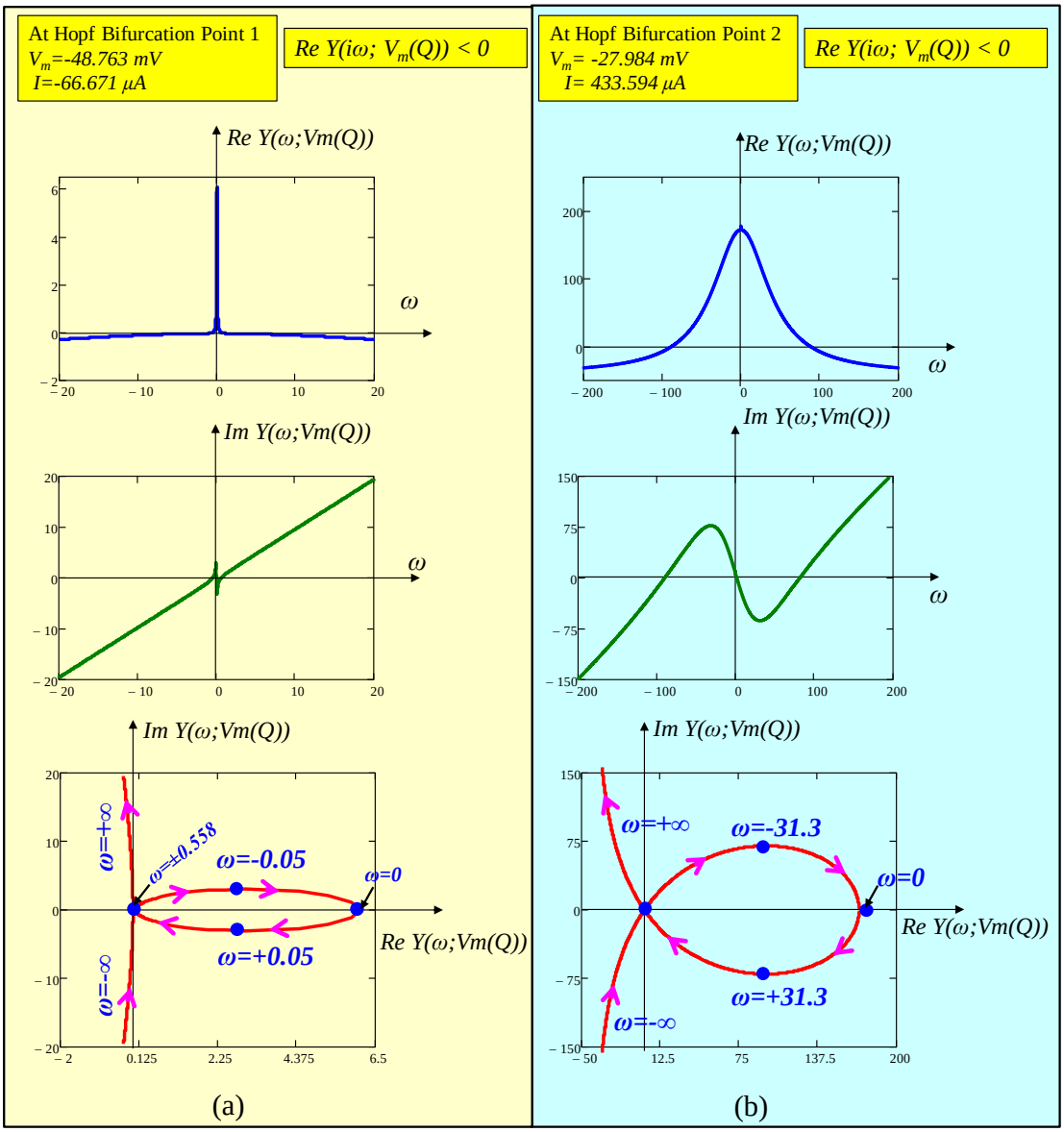

Figure 14. Small-signal admittance frequency response and Nyquist plot of the memristive Chay neuron model at (a) V_m= *-48.763 mV(resp., I= -66.671 μA)* and (b) V_m=*-27.984 mV(resp.*, I=*433.594 μA)*. Observe that *ReY(iω;V_m(Q))<0* at the two Hopf-bifurcation points.

5.4.2. Pole-zero diagram of the small-signal admittance function Y(s; Vm(Q)) and eigen values of the jacobian matrix

The location of the poles and zeros of the small signal admittance function $Y(s; V_m(Q))$ of (12a) is computed by factorizing it's denominator and numerators as

$$Y(s; V_m(Q)) = \frac{k(s-z_1)(s-z_2)(s-z_3)}{(s-p_1)(s-p_2)} \quad (13)$$

The poles of the small-signal admittance function $Y(s; V_m(Q))$ as a function of the voltage V_m over $-200\ mV<Vm<200\ mV$ is shown in Fig. 15. Observe from Fig. 15(a) and Fig. 15(b) that the two poles $Re(p_1)$, $Re(p_2)$ are negative while $Im(p_1)$, $Im(p_2)$ remain consistently zero for the specified DC input V_m. This observation confirms that the two poles of the admittance function possess no complex frequencies.

Fig. 16(a) shows the *Nyquist plot*, i.e. loci of the imaginary part $Im(z_i)$ *versus* the real part $Re(z_i)$ of the zeros as a function of the input voltage V_m over the interval $-55\ mV \le V_m \le 25mV$. Observe that the real part of the two zeros z_2 and z_3 are zero at V_m= *-48.763 mV(resp., I= -66.671 μA)* and V_m=*-27.984 mV(resp.,* I=*433.594 μA),* respectively. The corresponding points when $Re(z_i)=0$ are known as Hopf bifurcation points in bifurcation theory. Fig. 16(b) and Fig. 16(c) show the zoomed version of Fig. 16(a) near to the two bifurcation points respectively. It is also observed that the $Re(z_2)$ and $Re(z_3)$ lie in open right half plane(RHP) between the bifurcation points $-48.763\ mV <V_m<-27.984\ mV$(resp. *-66.671 μA <I < 433.594 μA).* Observe from Fig. 17 that the eigenvalues, computed from the Jacobian matrix, associated to the ODE (1a)-(1c) are identical to the zeros of the neuron local admittance $Y(s; V_m(Q))$, as inferable from Fig. 16, and expected from the Chua theory [3]-[4].

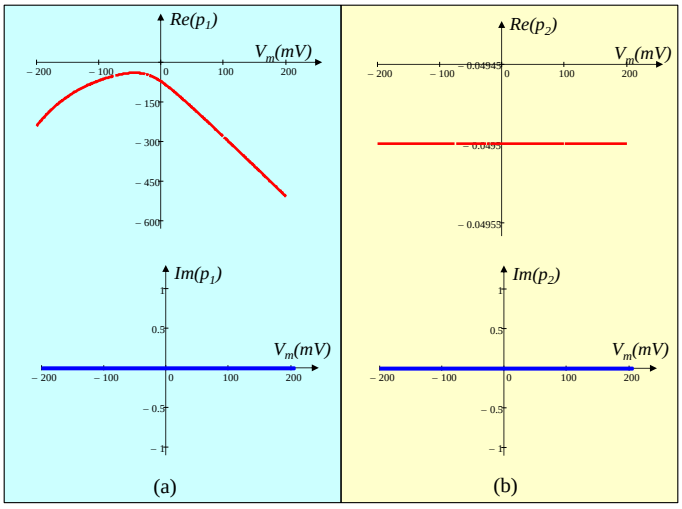

Figure 15. Poles diagram of the small-signal admittance function $Y(s; V_m(Q))$ as a function of V_m over $-200\ mV<V_m<200\ mV$ (a) Top and bottom figures are the plot of the real part of the pole 1 $Re(p_1)$ and Imaginary part of pole 1 $Im(p_1)$ respectively. (b) Top and bottom figures are the plot of the real part of the pole 2 $Re(p_2)$ and Imaginary part of pole 2 $Im(p_2)$ respectively.

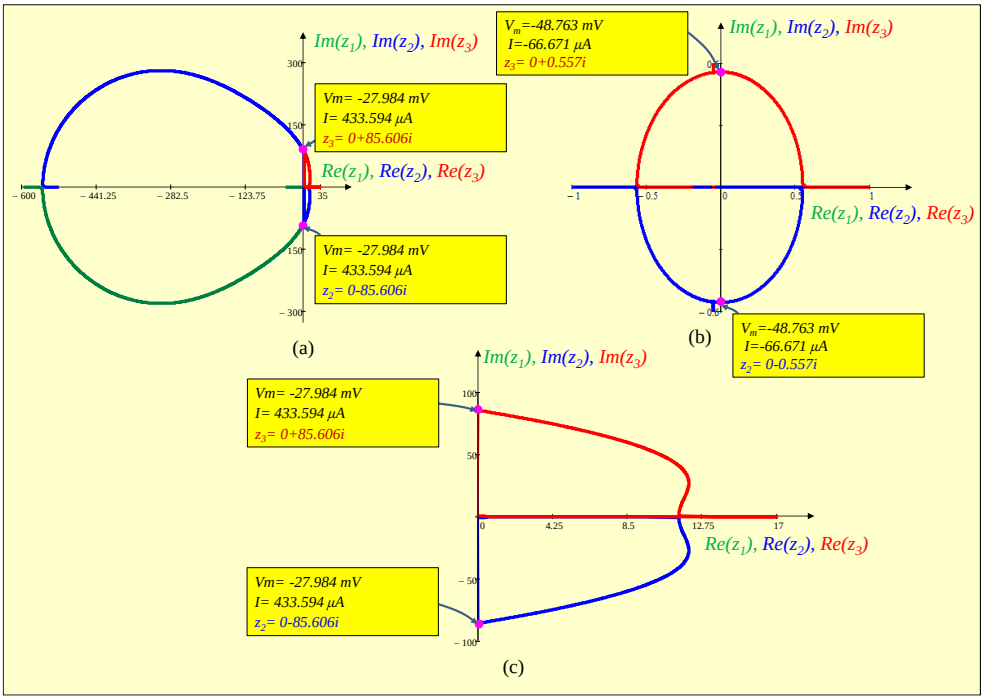

Figure 16. Zeros diagram of the small-signal admittance function *Y(s; Vm(Q))* (a) Nyquist plot of the zeros z_1, z_2, z_3 in *Im(zi) vs. Re(zi)* plane (b) Nyquist plot near the Hopf-bifurcation point 1, *Vm=-48.763 mV(resp., I= -66.671μA).* (c) Nyquist plot near the Hopf-bifurcation point 2, *Vm=-27.984 mV(resp., I=433.594 μA).*

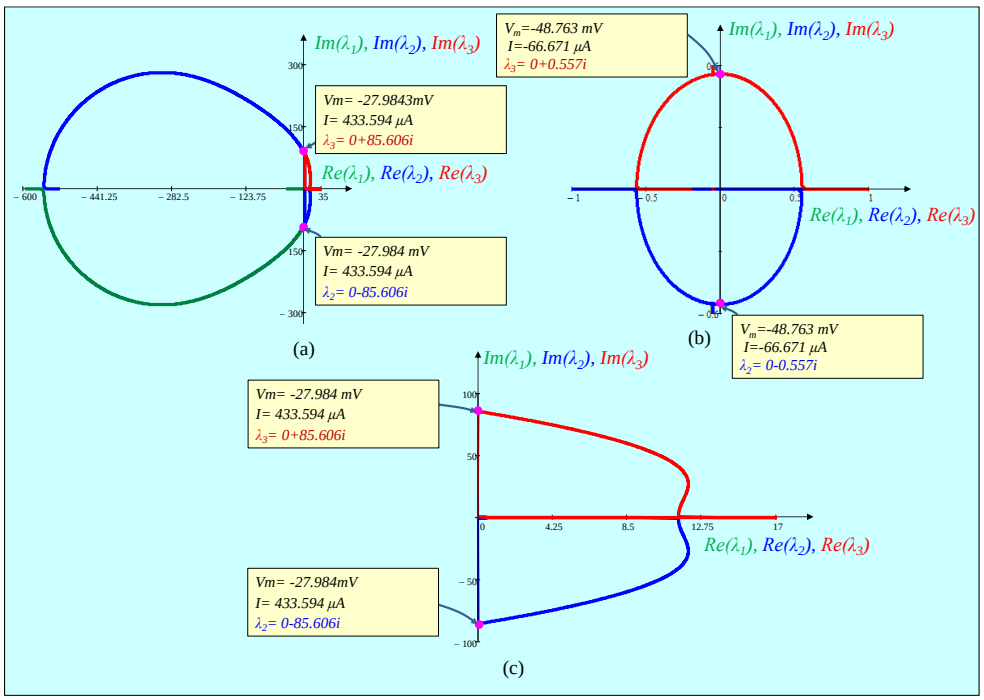

Figure 17. Plot of the loci of the eigen values of the Jacobian Matrix (a) Nyquist plot of the eigen values λ_1, λ_2, λ_3 in *Im(λi) vs. Re(λi)* plane Nyquist plot near the Hopf-bifurcation point 1, *Vm=-48.763 mV(resp., I= -66.671 μA).* (c) Nyquist plot near the Hopf-bifurcation point 2, *Vm=-27.984 mV(resp., I=433.594 μA).* Our numerical computations confirm the zeros of the admittance functions *Y(s; Vm(Q))* obtained in Fig. 16 are identical to the eigen values of the Jacobian matrix

6. Local Activity, Edge of Chaos and Hopf-Bifurcation in Memristive Chay Model

Local Activity and edge of chaos are the powerful mathematical quantitative theories to predict whether the nonlinear system exhibits complexity or not. Local activity refers to a characteristic of nonlinear systems wherein infinitesimal fluctuations in energy are amplified, leading to the emergence of complex dynamical behavior in the system [34-39]. This section presents an extensive analysis of the memristive Chay model using the principle of local activity, edge of chaos and Hopf-bifurcation theorem to predict the mechanism of generating the complicated electrical signals in an excitable cell.

6.1. Locally active regime

The local activity theorem developed by Chua reveals that a nonlinear system must satisfy at least one of the following conditions, concerning its local transfer function about a given operating point in order to support the emergence of complexity[36].

(i) The zero of the admittance function $Y(s; V_m(Q))$ lie in open-right plane where $Re(s_z)>0$

(ii) $Y(s; V_m(Q))$ has multiple zero on the imaginary axis

(iii) $Y(s; V_m(Q))$ has simple zero on the imaginary axis $s = i\omega_z$ on the imaginary axis and $K_Q(i\omega_z) \triangleq \lim_{s\to i\omega_z} = (s - i\omega_z)Y\left(s;\ V_m\left(Q\right)\right)$ is either a negative real number, or a complex number.

(iv) $ReY(i\omega;V_m(Q))<0$ for some $\omega\in[-\infty, +\infty]$

In another words, the emergence of action potentials, oscillations, chaos, burstings or spikes in neurons are impossible unless the cells are locally active. Therefore, restricting the behavior of a nonlinear system to its local activity operating regime reduces the considerable time necessary to identify the complex phenomena, which may emerge across its physical medium as compared to a standard trial-and-error numerical investigation. In order to restrict the above dynamical behavior in memristive Chay model of an excitable cell in local activity regime, we performed comprehensive numerical analyses within the range of the DC equilibrium voltage V_m*= -50 mV (resp. I= -74.316 μA)* to V_m*=-23.5 mV (resp. I= 1.76×10³ μA)*. Observe from Fig. 18(a), the real part of the admittance of the frequency response $ReY(i\omega; Vm(Q))>0$ at V_m*= -50 mV (resp. I= -74.316 μA)*, thereby confirming locally passive at this equilibrium point. However, when V_m*>-50mV*, our in depth simulation in Fig. 18(b) shows that $ReY(i\omega;Vm(Q))=0$ *at* V_m*= - 49.455 mV (resp. I= -70.919 μA)* and Fig. 18(c) and Fig. 18(d) show that $ReY(i\omega; Vm(Q))< 0$ at V_m*= -48.1 mV(resp. I= -62.681 μA)* and V_m*= -26.5 mV (resp. I=746.457 μA)* respectively for some frequency ω, confirming an excitable cell is locally active at these equilibria. Our simulations in Fig. 18(e) shows, a further increase in the DC equilibrium voltage at V_m*= -24.685 mV (resp. I=1.291×10³ μA)*, the loci is tangential to the ω axis i.e. $Re\ Y\ (i\omega; Vm(Q))=0$. However, when V_m*>-24.685 mV*, say V_m*=-23.5 mV(resp. I= 1.76×10³ μA)*, it is observed from Fig. 18(f) that Re $Y\ (i\omega; Vm(Q))>0$, and the memrisitve Chay model is no more locally active confirming the cell is locally passive at this equilibrium. Therefore, the local activity

regime which started above V_m=- *49.455 mV (resp. I= -70.919 μA)* exists over the following regime

Local Activity Regime
$-49.455\ mV < V_m < -24.685\ mV$
$-70.919\ \mu A < I < 1.291\times10^3\ \mu A$

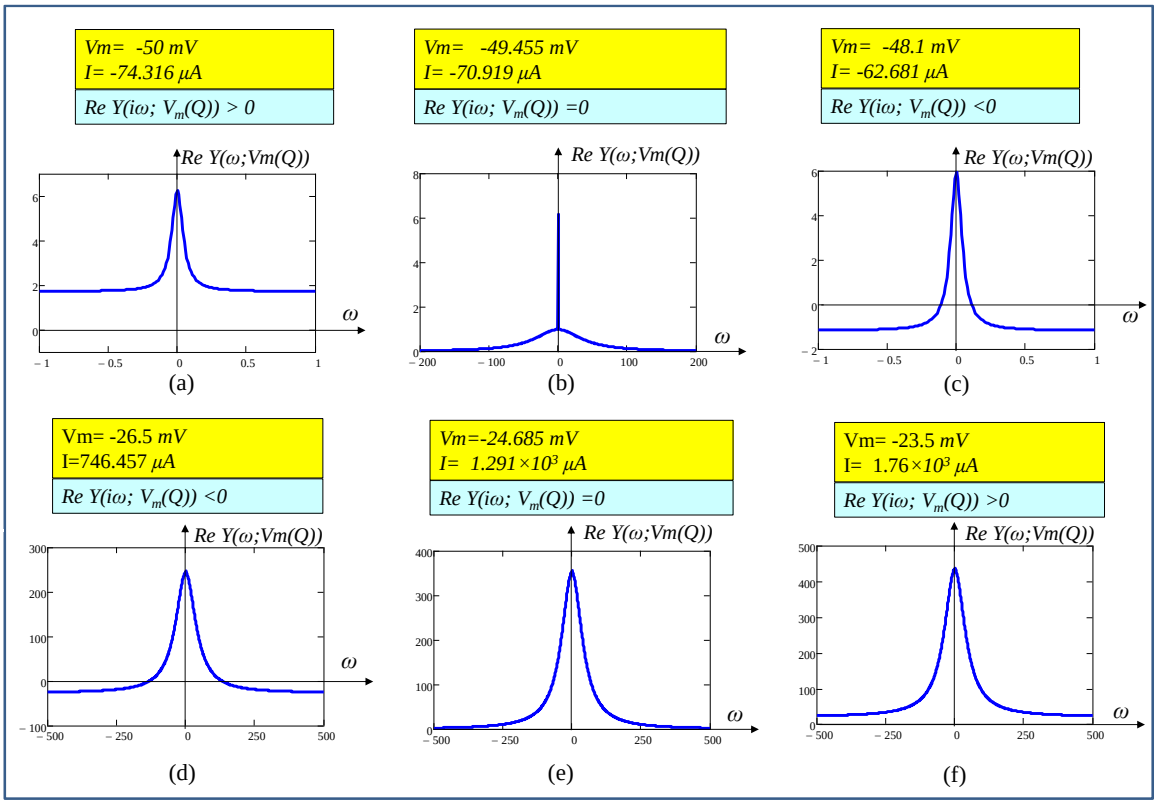

Figure 18. Plot of *Re(iω; Vm(Q))* to illustrate the local activity principle at (a) V_m= *-50 mV (resp. I= -74.316 μA)* (b) V_m= *- 49.455 mV (resp. I= -70.919 μA)*, (c) V_m= *-48.1 mV(resp. I= -62.681 μA)*, (d) V_m= *-26.5 mV (resp. I=746.457 μA)*, (e) V_m= *-24.685 mV (resp. I=1.291×10³ μA)*, (f) V_m=*-23.5mV(resp. I= 1.76×10³ μA)*, respectively.

6.2. Edge of chaos regime

Edge of chaos is a tiny subset of the locally-active domain where the zeros of the admittance function *Y(s; Vm(Q))*(equivalent to the eigen values of Jacobian matrix) lie in the open left-half plane, i.e. Re(z_p)<0(eigen values λi<0) as well as *ReY(iω; Vm(Q))<0*. Fig. 17(a) and Fig. 17(b) show the real part of the *eigen values* vanish at V_m=*-48.7631 mV* (resp. *I=-66.671 μA*) with pair of complex eigen values $\lambda_{2,3}$= ± 0.557i. It follows from the edge of chaos theorem that the corresponding equilibrium point is no longer *asymptotically* stable, and becomes unstable thereafter confirming the *1st edge of chaos* regime over the following small interval:

Edge of chaos domain 1
$-49.455\ mV < V_m < -48.763\ mV$
$-70.919\ \mu A < I < -66.671\ \mu A$

Observe from Fig. 17(c) that the real part of the eigen values vanish at $\lambda_{2,3} = \pm 85.606i$ *at* DC equilibrium voltage $V_m = -27.984\ mV$(resp. $I = 433.594\ \mu A$). It follows that the corresponding equilibrium point $V_m(Q)$ is no longer *asymptotically* stable below this equilibrium point, therefore confirming the existence of a *2nd edge of chaos* regime over the following interval:

Edge of chaos Domain 2
$-27.984\ mV < V_m < -24.685\ mV$
$433.594\ \mu A < I < 1.291\times 10^3\ \mu A$

The nonlinear dynamical behavior of the memristive Chay model in this paper is controlled as the function the input stimulus I. The local activity, edge of chaos 1 and edge of chaos 2 regime computed in this paper under the assumption of departing the input parameter *I* from lower stimulus to higher stimulus (resp. low DC equilibrium voltage $V_m(Q)$ to high equilibrium voltage $V_m(Q)$).

6.3. Hopf-bifurcation

Hopf-bifurcation namely, *super-critical* and *sub-critical* bifurcations are local bifurcation phenomenon in which an equilibrium point changes its stability as the parameter of the nonlinear system changes under certain conditions. When an unstable equilibrium point surrounded by a stable limit cycle results to a super-critical Hopf bifurcation whereas a subcritical Hopf bifurcation refers to a qualitative change in the behavior of a system where a stable equilibrium point transitions to instability, giving rise to sustained oscillations or limit cycles as a parameter is varied. Our careful simulation at Hopf-bifurcation point 1 at $V_m = -48.763\ mV$(resp. $I = -66.671\ \mu A$)[8] shows that stimulus current *I* should be chosen within very small edge of chaos domain 1, where the real part of the eigen values are negative, the result converges to DC equilibrium for any initial conditions. Likewise, *I* is selected within the bifurcation point 1, where the real part of eigen values are positive, the result converges to a stable limit cycle. Therefore, it follows from the bifurcation theory that bifurcation point 1 is a super-critical Hopf bifurcation. Fig. 19(a) and Fig. 19(b) show the numerical simulations at $I = -68.118\ \mu A$ and $I = -65.077\ \mu A$ respectively. Observe, from Fig. 19(a) and Fig. 19(b) that $I = -68.118\ \mu A$ lying within the tiny subset of edge of chaos domain 1 converges to DC equilibrium and $I = -65.077\ \mu A$ lying in open right half-plane(RHP) converges to a spikes, respectively, confirming the bifurcation point 1 is a super-critical Hopf bifurcation.

[8] The super critical Hopf bifurcation point 1 and point 2 observed in this paper are just for the parameters listed in Table 2. The bifurcations phenomenon may vary for different parameters.

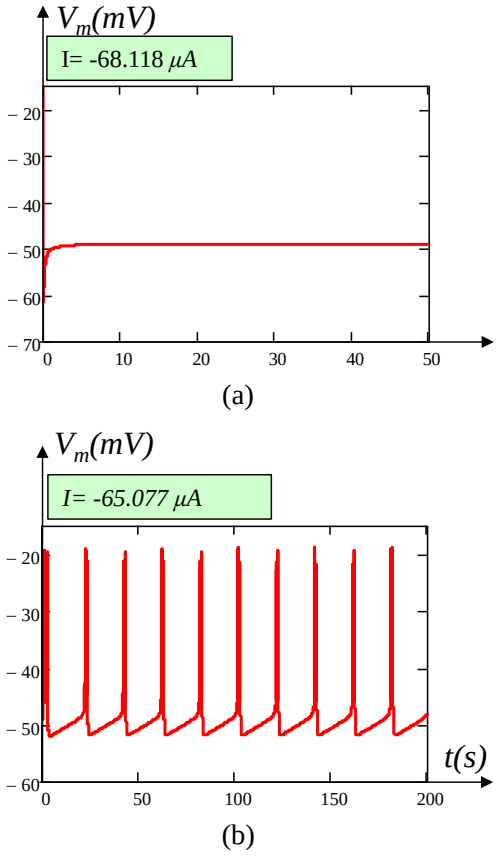

Figure 19. Numerical simulations to confirm the super-critical Hopf bifurcation at bifurcation point 1. Plot of membrane potential V_m at (a) *I= -68.118 μA* which lies inside the tiny subset of edge of chaos domain 1 and beyond bifurcation point 1 converges to the DC equilibrium, (b) and *I= -65.077 μA*, chosen just to the right of bifurcation point 1, where the real parts of two zeros of the neuron local admittance lie on the open right half plane (RHP) converges to the spikes

Similarly, our careful examination predicts a stable DC equilibrium point when current *I* is chosen within a very small edge of chaos 2, confirming supercritical Hopf bifurcation at bifurcation point V_m*= -27.984 mV (resp. I= 433.594 μA)*. The possibility of above scenario is illustrated in Figs. 20. Fig. 20(a) shows the membrane potential V_m converges to stable DC equilibrium point when *I=440 μA* chosen within the edge of chaos domain 2. Fig. 20(b) shows when *I=430.884 μA* chosen very close and inside the bifurcation point 2, where the real part of the eigen value is positive and lie in open right half plane(RHP), the transient waveform converges to stable limit cycle as predicted by Hopf supercritical bifurcation theorem.

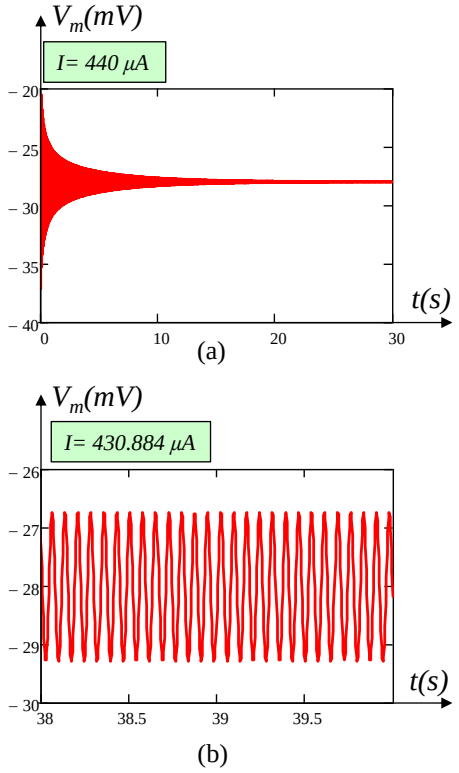

Figure 20. Numerical simulations to confirm the super-critical Hopf bifurcation at bifurcation point 2. (a) Plot of membrane potential V_m which converges to stable DC equilibrium when $I=440\ \mu A$ chosen inside the tiny subset of edge of chaos domain 2 and, near and beyond the bifurcation point 2. (b) Membrane potential converging to oscillation as predicted by Hopf bifurcation theorem when $I=430.884\mu A$ is chosen inside the bifurcation point (open right-half pane).

Table 7 illustrates the computation of the potassium ion-channel activation n, calcium concentration Ca and eigen values (λ_1, λ_2 and λ_3) as a function of the DC stimulus current I (resp. membrane potential V_m) at the DC equilibrium point Q. It is observed from Table 7 and Fig. 17(a) to Fig. 17(c) that the two Hopf bifurcations points 1 and 2 occur at $Vm= =-48.763\ mV$(resp. $I=-66.671\ \mu A$) and $V_m= -27.984\ mV$ (resp. $I= 433.594\ \mu A$) respectively, where the eigen values are purely imaginary at these two equilibria. As I decreases (resp. V_m decreases) from the Hopf bifurcation point 1, the eigen values migrated to the left-hand side confirming the real parts of the eigen values are no longer positive and thereby confirming the first negative real eigen values regime exists over the following interval.

Negative real eigen values regime 1 :

$$-\infty < V_m < -48.763\ mV$$

$$-\infty < I < -66.671\ \mu A$$

Similarly, as I increases(resp. V_m *increases*) from the second bifurcation points, the positive real part of the eigen values migrated from open right half to the open left half, there by confirming the second negative real eigen values regime over the following

interval:

$$\boxed{\begin{array}{c} \textit{Negative real eigen values regime 2 :} \\ -27.984\ mV < V_m < +\infty \\ 433.594\ \mu A < I < +\infty \end{array}}$$

Table 7. Computation of the potassium ion-channel activation *n*, calcium concentration *Ca* and eigen values (λ_1, λ_2 and λ_3) as a function of the stimulus current *I* (resp. membrane potential V_m). Rows 5 to 7 pertain to the edge of chaos 1, rows 8 to 16 pertain to the unstable local activity domain and rows 17 to 20 pertain to the edge of chaos 2. Rows 7 and 17 pertain to Hopf bifurcation point 1 and Hopf bifurcations points 2, respectively for the memristive Chay neuron model.

S. N	V_m(Vm)	**I(μA)**	**n**	**Ca**	λ_1	λ_2	λ_3
1.	-52.00	-87.02	0.08	0.04	-40.515	-3.842	-0.084
2.	-51.00	-80.63	0.08	0.05	-40.107	-2.871	-0.111
3.	-50.50	-77.46	0.09	0.06	-39.891	-2.289	-0.139
4.	-50.00	-74.32	0.09	0.07	39.666	-1.617	-0.196
5.	-49.455	-70.919	0.94	0.08	-39.408	-0.533-0.174i	-0.533+0.174i
6.	-49.00	-68.12	0.1	0.1	-39.181	-0.19-0.525i	-0.19+0.525i
7.	-48.763	-66.671	0.1	0.1	-39.058	0-0.557i	0+0.557i
8.	-48.50	-65.08	0.1	0.11	-38.917	0.222-0.51i	0.2215+0.5097i
9.	-46.00	-51.02	0.12	0.21	-37.32	0.046	5.736
10.	-45.00	-46.37	0.13	0.27	-36.512	0.027	8.498
11.	-42.00	-39.37	0.16	0.53	-33.218	0.0001	18.604
12.	-40.00	-42.78	0.18	0.79	-29.899	-0.0084	25.99
13.	-38.00	-51.26	0.21	1.13	-24.898	-0.0112	31.992
14.	-32.00	17.59	0.29	2.57	-0.061	11.669-38.01i	11.669+38.01i
15	-30.00	160.68	0.32	3.12	-0.053	8.049-61.778i	8.049+61.778i
16.	-28.00	430.84	0.35	3.65	-0.051	0.08-85.421i	0.08+85.421i
17.	-27.984	433.594	0.35	3.65	-0.051	0-85.606i	0+85.606i
18.	-27.00	628.91	0.36	3.89	-5.556-97.197i	-5.556+97.197i	-0.051
19.	-25.50	1.02×10^3	0.39	4.22	-15.942-114.607i	-15.942+114.607i	-0.0501
20.	-24.685	1.291×10^3	0.40	4.37	-22.466-123.858i	-22.466+123.858i	-0.0499
21	-23.00	1.99×10^3	0.43	4.64	-37.643-142.384i	-37.643+142.384i	-0.0497
22	-22.00	2.5×10^3	0.44	4.75	-47.529-152.923i	-47.529+152.923i	-0.0496

Observe from Table 7 and Fig. 17(a)-Fig. 17(c) that two eigenvalues of the Jacobian matrix associated to the ODE set (1a)-(1c) lie on the open RHP for each operating point Q corresponding to a DC current *I* value between Hopf bifurcation point 1 and Hopf bifurcation point 2. Therefore, the generation of periodic, bursting, spikes and chaos signals

predicted by Hopf bifurcation theorem in an excitable cell exists over the following interval:

$$\begin{array}{c} \textit{Unstable (periodic, bursting, chaos, spikes) regime :} \\ -48.763\ mV < V_m < -27.984\ mV \\ -66.671\ \mu A < I < 433.594\ \mu A \end{array}$$

The convergence of the membrane potential to a stable and unstable DC equilibrium points are verified by numerical simulations at different values of I and are illustrated in Figs. 21. Fig. 21(a) shows the transient waveform of membrane potential V_m converging to a stable DC equilibrium at I= *-90 μA*, confirming the Hopf bifurcation theorem no longer holds at this equilibrium. Similarly, when DC simulus currents I= *-50 μA* and *-10μA* are chosen inside the two bifurcation points *I=-66.671 μA* and *I= 433.594 μA*, we observed different patterns of oscillations as shown in Fig. 21(b) and Fig. 21(c), confirming the bifurcation theorem holds in this regime. Likewise, when DC stimulus currents *I=10 μA* and *I=2000μA* are applied within the bifurcation points *I=−66.671 μA* and *I=433.594*, respectively, oscillation patterns emerge as depicted in Fig. 22(a) and Fig. 22(b). Similarly, Fig. 22(c) illustrates the transient waveform of the membrane potential V_m, indicating its convergence to a stable DC equilibrium at *I=500 μA*. This observation suggests that the Hopf bifurcation theorem no longer holds at this equilibrium point.

Figs. 23 and Figs. 24 show the different patterns of oscillations when the conductance g_{KCa} of calcium sensitive potassium ion channel memristor is varied from *10 mS/cm²* to *11.5 mS/cm²* at *stimulus current I=0*. Fig. 23(a) shows the excitable membrane cell has a stable limit cycle with period one at $g_{K,Ca}$*=10 mS/cm²*. As the parameter $g_{K,Ca}$ increases to 10.7 *mS/cm²*, 10.75 *mS/cm²*and 10.77 *mS/cm²* the cell fires period two, four and eight as shown in Fig. 23(b), Fig. 23(c) and Fig. 24(a) respectively. The change in the period doubling is more apparent in calcium *concentration (Ca) vs. time* and, V_m *vs. Ca* as shown in the bottom of Fig. 23(b), Fig. 23(c) and Fig. 24(a) respectively. Fig. 24(b) shows the waveform of the memrisive Chay model confirming the existence of aperiodic oscillation (chaos) at $g_{K,Ca}$*=11 mS/cm²*. The firing of aperiodic oscillations from cell can be clearly seen from the plot of the *Ca vs. time* and V_m *vs. Ca* in Fig. 24 (b). A further increase in $g_{K,Ca}$ to 11.5 *mS/cm²* gives rise to the firing of the cell from aperiodic to rhythmic bursting as shown in Fig. 24(c).

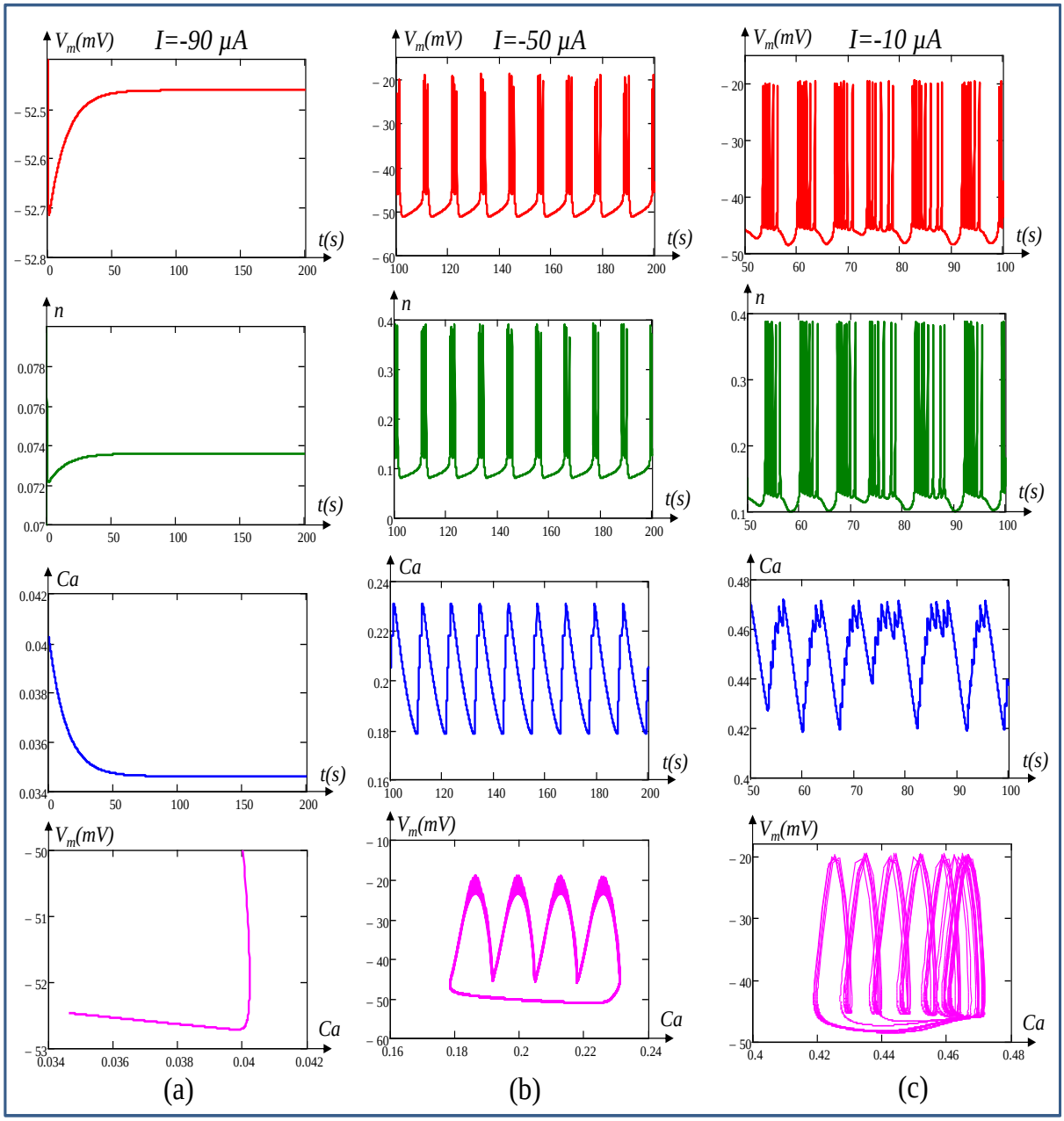

Figure 21. Patterns of oscillations when stimulus current *I* is chosen beyond and inside the bifurcations points. (a) DC pattern observed when *I= -90 μA* chosen beyond bifurcation point 1*(I=-66.671 μA).* Different patterns of oscillatiions when *I* is chosen between the two bifurcation points *I=-66.671 μA* and *I= 433.594 μA,* at (b) *I= -50 μA,* (c) *I= -10 μA.*

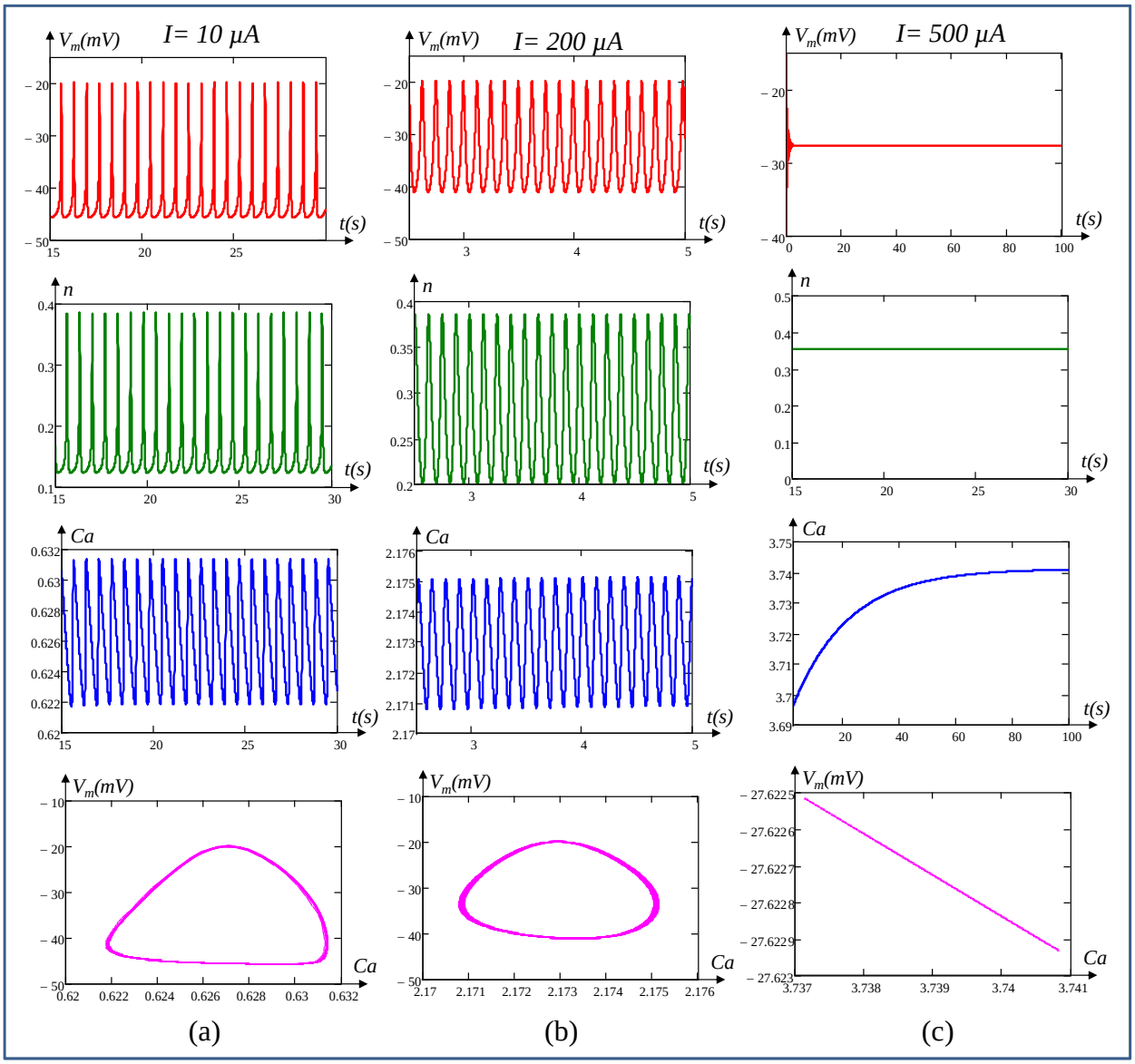

Figure 22. Patterns of oscillations when stimulus current *I* is chosen inside and beyond the bifurcations points. Oscillatiions patterns when *I* is chosen between the two bifurcation points *I=-66.671 μA* and *I= 433.594 μA*, at (a) *I=10 μA*, and (b*) I=200 μA. (c)* DC pattern when *I=500 μA* is chosen beyond the bifurcation point 2(*I = 433.594 μA).*

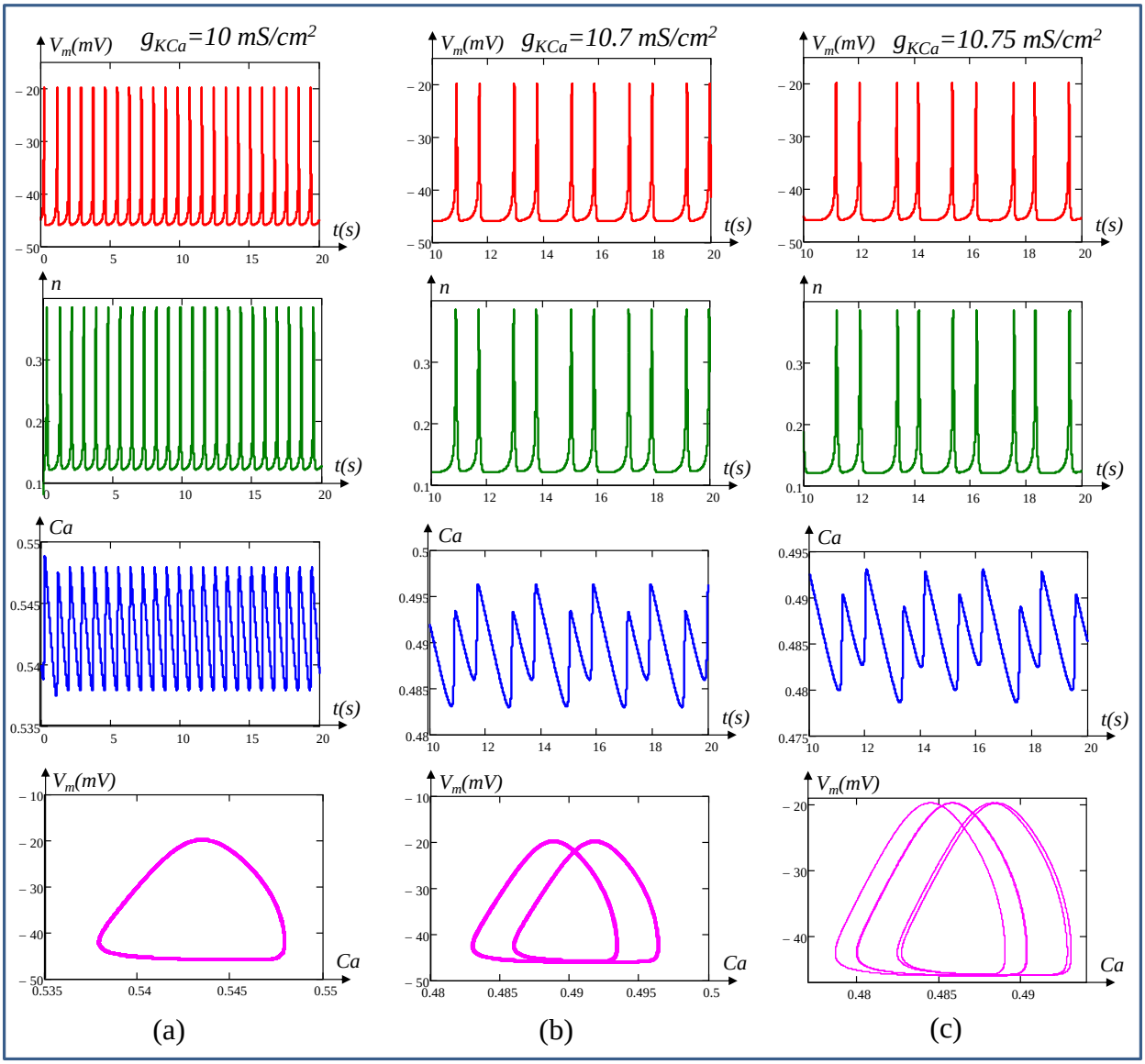

Figure 23. Different patterns of oscillations when g_{KCa} varied from *10 mS/cm²* to *10.75 mS/cm²* at DC situmulus current *I=0*. (a) Period-1 oscillation at $g_{K,Ca}$*=10 mS/cm²* (b) Period-2 oscillation at $g_{K,Ca}$*=10.7 mS/cm²* (c) Period-4 oscillation at $g_{K,Ca}$*=10.75 mS/cm²*. The simulations were performed at the initial conditions $V_m(0)$*=-50mV*, *n(0)=0.1* and *Ca(0)=0.48*.

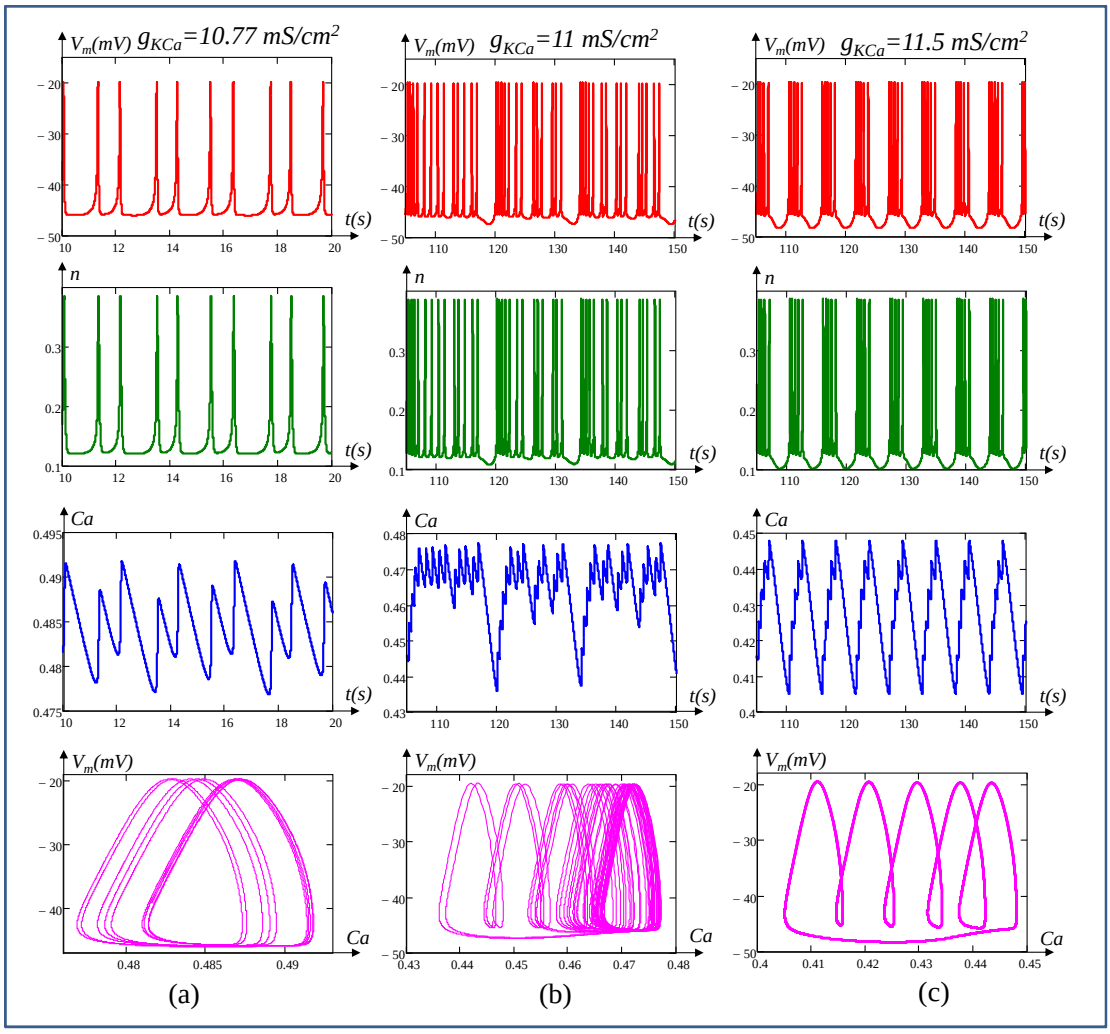

Figure 24. Different patterns of oscillations when g_{KCa} varied from *10.77 mS/cm²* to *11.5 mS/cm²* at DC stimulus current *I=0*. (a) Period-8 oscillation at $g_{K,Ca}$*=10.77 mS/cm²* (b) Aperiodic (chaotic) oscillation at $g_{K,Ca}$*=11 mS/cm²* (c) Bursting at $g_{K,Ca}$*=11.5 mS/cm²*. The simulations were performed at the initial conditions $V_m(0)$*=-50mV*, *n(0)=0.1* and *Ca(0)=0.48*.

7. Concluding Remarks

This paper has provided a comprehensive and quantitative analysis of a biological excitable cell using the Chay neuron model. Through memristive theory, we have demonstrated that the *voltage-sensitive mixed ion-channel* functions as a nonlinear resistor, while the *voltage-sensitive potassium ion-channel* and *calcium-sensitive potassium ion-channel* in an excitable cell are indeed time-invariant first-order generic memristors.

Furthermore, we have conducted in-depth analyses to derive the small signal model, admittance function, pole-zero diagram, frequency response of admittance functions, and Nyquist plot at the DC equilibrium point Q. Our investigations revealed the existence of the local activity regime in the memristive Chay model within the voltage range of *-49.455 mV to -24.685 mV*, and identified edge of chaos regime domains 1 and 2 within the voltage ranges of *-49.455 mV to -48.763 mV*, and *-27.984 mV to -24.685 mV*, respectively.

Moreover, consistent with the predictions of the Hopf bifurcation theorem, we observed the presence of an oscillating regime between two bifurcation points within the voltage range of *-48.763 mV to -27.984 mV*. Our numerical simulations confirmed the super-critical Hopf bifurcation with complex conjugates of eigenvalues coincide on the purely imaginary axis at $\pm 0.557i$ and $\pm 85.606i$ respectively. It was also observed that a tiny change in external stimulus current I in excitable cells, far from the bifurcation points no longer holds the Hopf bifurcation theorem as it crosses the imaginary axis from right to left confirming that the real part of the eigenvalues becomes negative and converges to a DC equilibrium point.

Our comprehensive comparison of the HH, FitzHugh-Nagumo, ML, and the Chay models presented in Table 2 along with their individual strengths and limitations reveals distinct advantages and drawbacks making them suitable for different research contexts and questions. The selection of the particular model depends on the specific objectives. We primarily focused to advance the understanding of excitable cells by modeling with the networks of memristors and predicting their responses with the concept of memristor theory, DC steady state analyses, small signal equivalent circuit, local activity principle, edge of chaos theorem and hopf bifurcations. In Conclusion, the theoretical framework outlined in this paper confirms the significance of memristors in simulating action potentials in excitable cells and also establishes a foundation for their application in neuron modeling, artificial intelligence, and brain-like machine interfaces. Our proposed model offers potential for enhancing adaptive neural networks, neuroprosthetics, neuromorphic computing architectures, and the broader scope of artificial intelligence, thereby aiding in the development of brain-like information processing systems.

Appendix: Abbreviations of the Model Parameters

C_m=Membrane Capacitance
E_K =Potential across K^+ ion channel memristor
E_I =Potential across mixed ion channel memristor
E_L =Potential across leakage channel
E_{Ca} =Potential across Ca^{+2} ion channel memristor
$g_{K,V}$ =Voltage-sensitive K+ ion-channel conductance
g_I =Voltage-sensitive mixed ion channel conductance
g_L =Leakage channel conductance
g_{KCa} =Calcium activated potassium conductance
k_{Ca} =Rate constant for the efflux of the intracellular Ca^{+2} ions
ρ =Proportionality constant
λ_n =Rate constant for k^+ ion-channel opening

m_∞= Probability of activation of the mixed ion channel in steady state
α_m= The rate at which the activation of the mixed ion channel closed gates transition to an open state(s^{-1})
β_m= The rate at which the activation of the mixed ion channel open gates transition to the close state(s^{-1})

h_∞= Probability of inactivation of the mixed ion channel in steady state
α_h=The rate at which the inactivation of the mixed ion channel closed gates transition to an open state(s^{-1})
β_h=The rate at which the inactivation of the mixed ion channel open gates transition to the close state(s^{-1})

n=Probability of n opening of the K+ ion channel memristor
n_∞ =Steady state value of n
α_n=The rate at which K^+ ion channel closed gates transition to an open state(s^{-1})
β_n=The rate at which K^+ ion channel opened gates transition to an close state(s^{-1})

Author Contributions: All authors have read and agreed to the published version of the manuscript.

Funding: This research received no external funding.

Data Availability Statement: Not applicable.

Conflicts of Interest: The authors declare no conflict of interest.

References

1. Hodgkin, A.L.; Huxley, A.F. A quantitative description of membrane current and its application to conduction and excitation in nerve. *J. Physiol* **1952,** 117, 500-544.
2. Chua, L.O.; Kang, S.M. Memristive devices and systems. *Proc. the IEEE*. **1976**, 64, 209-223.
3. Chua, L.O; Sbitnev, V.I.; Kim, H. Hodgkin-Huxley axon is made of memristors. *Int. J. Bifurcation and Chaos.* **2012**, 22, 1230011(1) - 1230011.
4. Chua, L.O.; Sbitnev, V.I.; Kim, H. Neurons are poised near the edge of chaos. *Int. J. Bifurcation and Chaos*. **2012,** 22, 1250098 (1) - 1250098 (49).
5. Chua, L. Hodgkin–Huxley equations implies Edge of chaos kernel. Jpn. J. Applied Physics. **2022,** 61(SM) SM0805(1)-(36).
6. Chua, L. Everything you wish to know about memristor but are afraid to ask. *Radioengineering*. **2015,** 24, 319-368.
7. Hodgkin, A.L.; Keynes, R.D. Experiments on the injection of substances into squid giant axons by means of microsyringe. *J. Physiol*. **1956,** 131, 592-616.
8. Morris, C.; Lecar, H. Voltage oscillations in the Barnacle giant muscle fiber. *J. of Biophysical Society*. **1981,** 35, 193-213.
9. Sah, M.P.; Kim, H.; Eroglu, A.; Chua, L. Memristive model of the Barnacle giant muscle fibers. *Int. J. Bifurcation and Chaos*. **2016,** 26, 1630001 (1)-(40).
10. Rajamani, V.; Sah, M.P.; Mannan, Z.I.; Kim, H.; Chua, L. Third-order memristive Morris-Lecar model of barnacle muscle fiber. *Int. J. Bifurcation and Chaos*. **2017**, 27, 1730015 (1)-(58).
11. Noble, D. A modification of the Hodgkin-Huxley equations applicable to Purkinje fibre action and peacemaker potentials. *J. of Physiology*. **1962**, 160, 317-352.
12. Hudspeth, A. J.; Lewis, R.S. A model for electrical resonance and frequency tuning in saccular hair cells of the bull-frog Rana catesbeiana. *J. Physiology*. **1988**, 400, 275-297.
13. Giguère, C.; Woodland, P.C. A computational model of the auditory periphery for speech and hearing research. *The Journal of the Acoustical Society of America*. **1994,** 95, 331-342.
14. Nawrocki, R.A; Voyles, R. M.; Shaheen, S. E. A mini review of neuromorphic architectures and implementations. *IEE Transactions on Electron Devices*. **2016**, 63, 3819-3829.
15. Lee, Y; Lee, T. W. Organic synapses for neuromorphic electronics: from brain inspired computing to sensorimotor nervetronics. *American Chemical Society*. 2019, 52, 964–974.
16. Gentili, P. L. Photochromic and luminescent materials for the development of chemical artificial intelligence. *Dyes and Pigments*. **2022,** 205, 1-14.
17. Peercy, B. E, Sherman, A. S. How pancreatic beta-cells distinguish long- and short-time scale CAMP signals. *Biophys. J.* **2010**, 99. 398-406.
18. Pedersen. M. G. Contributions of mathematical modeling of Beta-cells to the understanding of beta-cell oscillations and insulin secretion. *Diabetes Technology Society*, **2009.** 3. 12-20.
19. Felix-Martınez, G. J.; Godlinez-Fernandez, J. R. *Mathematical models of electrical activity of the pancreatic β-cell. Islets.* **2014**. 6. e949195(1)- e949195(13).
20. Kaestner, K. H.; Thompson, M. C.; Dor, Y.; Gill, R. G.; Glaser, B.; Kim, S. K.; Sander, M.; Stabler, C.; , Stewart, A. F.; Powers, A. C. What is a β-cell ? -Chapter I in the Human Islet Research Network (HIRN) review series. *Molecular Metabolism*. **2021,** 53, 101323(1)- 101323 (6).
21. Lenzen, S. The pancreatic beta cell: an intricate relation between anatomical structure, the signalling mechanism of glucose-induced insulin secretion, the low antioxidative defence, the high vulnerability and sensitivity to diabetic stress. *ChemTexts.* **2021,** 7, 1-6
22. Marinelli, I.; Thompson, B. M; Parekh, V. S. Fletcher P. A. L. G. Giorda, A. S. Sherman, L. S. Satin, and R. Bertram, Oscillations in K(ATP) conductance drive slow calcium oscillations in pancreatic β-cells. *Biophysical Journal,* **2022**, 121, 1449-1464.
23. Marinelli, I.; Parekh, V.; Fletcher, P.; Thompson, B.; Ren, J.; Tang, Xi.; Saunders, T. L.; Ha, J.; Sherman, A.; Bertram, R.; Satin, L. S. Slow oscillations persist in pancreatic beta cells lacking phosphofructokinase M, *Biophysical Journal. 2022,* 121. 692-704.
24. Mukai, E.; Fujimoto, S.; Inagaki, N. Role of Reactive Oxygen Species in Glucose Metabolism Disorder in Diabetic Pancreatic β-Cells. *MDPI, Biomolecules. 2022,* 12091228(1)-(15).
25. Millette, K.; Rodriguez, K.; Sheng, X.; Finley, S. D.; Georgia, S. Exogenous Lactogenic Signaling Stimulates Beta Cell Replication In Vivo and In Vitro. *MDPI, Biomolecules*. **2022,** 12020215(1)-(10).
26. Bertram R.; Marinell, I.; Fletcher, P. A.; Satin, L. S.; Sherman, A.S. Deconstructing the integrated oscillator model for pancreatic *β*-cells, *Mathematical Biosciences.* **2023,** 365, 1-14.
27. Plant, R.E. Bifurcation and resonance in a model for bursting nerve cells. *Journal of mathematical biology*. **1981**, 11, 15-32.

28. Chay, T.R. Eyring rate theory in excitable membranes. Application to neural oscillations. *Journal of physical chemistry.* **1983,** 87, 2935-2940.
29. Chay, T.R.; Keizer, J. Minimal model for membrane oscillations in the pancreatic β-cell. *J. biophysical society*. **1983**, 42, 181-190.
30. Chay, T.R. Chaos in a three-variable model of an excitable cell. *Physics D.* **1985,** 16, 233-242.
31. FitzHugh, R. Impulses and physiological states in theoretical models of nerve membrane. *Biophysical Journal*. **1961,** 1, 445-466.
32. Chua, L. Five non-volatile memristor enigmas solved. *Applied Physics A Materials Science and Processing.* **2018,** 124, 563(1)-(43).
33. Chua, L. If it's pinched it's a memristor. *Semicond. Sci. Technol.* **2014,** 29, 104001(1)-104001(42).
34. Chua, L.O.; Desoer, C.A. Kuh E. S. Linear and Nonlinear Circuits . McGraw-Hill book Co. New York. **1987**.
35. Chua, L.O. CNN: A Paradigm for Complexity, World Scientific. **1998.**
36. Chua, L.O. Local activity is the origin of complexity. *Int. J. Bifurcation and Chaos.* **2005.** 15. 3435-3456.
37. Chua, L. O. Local activity principle: Chua's riddle, "Turing machine, and universal computing rule 137", in The Chua Lectures: From Memristors and Cellular Nonlinear Networks to the Edge of Chaos. *World Scientific Nonlinear Science Series A.* **2020.**
38. Ascoli, A.; Demirkol ,A.S.; Chua, L.O.; Tetzlaff, R. Edge of Chaos Theory Resolves Smale Paradox. *IEEE Trans. Circuit and System-I.* **2022**, 69, 1252-1265.
39. Sah, M.P.; Mannan, Z.I.; Kim, H.; Chua, L. Oscillator made of only One memristor and one battery. *Int. J. Bifurcation and Chaos.* **2015**, 25, 1530010(1)-(28).